Supplemental Data

Mechanism of Local
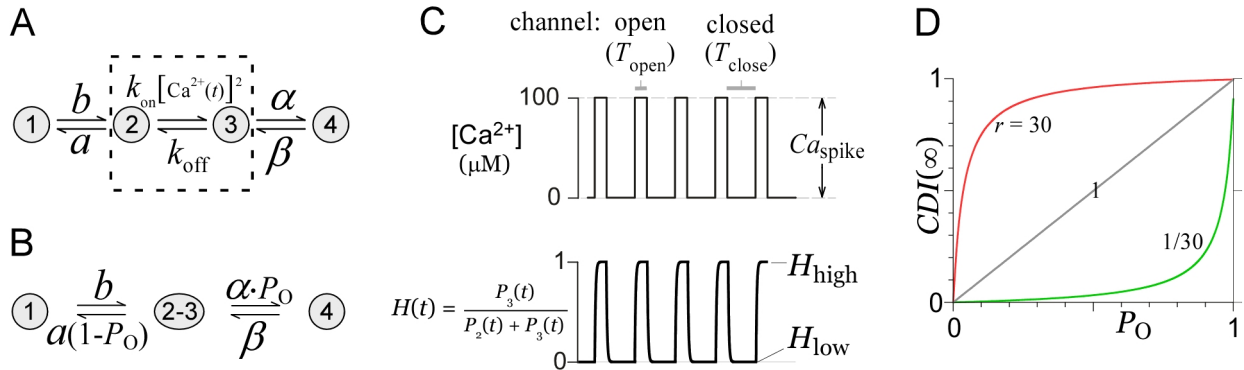
and Global Ca²⁺ Sensing by Calmodulin

in Complex with a Ca²⁺ Channel

Michael R. Tadross, Ivy E. Dick, and David T. Yue

1. Supplemental SQS Theory—Upward Curvature Strongly Distinguishes in Favor of SQS
1A. Derivation of main paper Equation 2; SQS analytic equation yields upward curvature if $r < 1$.

Figure S1 Analytic solution of the SQS mechanism. (A) Basic time-varying 4-state mechanism. (B) Equivalent time-invariant SQS mechanism. (C) Schematized Ca²⁺ signal under high buffering (top) and corresponding oscillations of fractional state 3 occupancy (bottom). Duration of channel opening (T_{open}) and closing (T_{close}) shown (top). (D) Steady-state SQS behavior.

The 'slow quick slow' SQS mechanism is a subclass of the basic system (Figure S1A of main paper Figure 2A) with three requirements. The first is 'quick' switching between states 2-3 (in both directions), where the probabilities of occupying states 3 and 2 must reach steady-state levels within the millisecond duration of a channel opening (T_{open}) and closing (T_{close}). As will be explained in Supplementary Information 2, this holds only when $k_{\text{on}} \cdot Ca_{\text{spike}}^2 + k_{\text{off}} \gg 1/T_{\text{open}}$ $\underline{\text{and}}$ $k_{\text{off}} \gg 1/T_{\text{close}}$. Second, there must be 'slow' switching between states 1-2, which is satisfied if $(a + b) \ll 1 / \min(T_{\text{open}}, T_{\text{close}})$, where the time constant of equilibration between states 1 and 2 is $1 / (a + b)$. Third is the requirement of 'slow' switching between states 3-4, i.e. $(\alpha + \beta) \ll 1 / \min(T_{\text{open}}, T_{\text{close}})$. The latter two conditions ensure that the probabilities of occupying states 1 and 4 cannot change significantly on the millisecond timescale of channel gating.

Under conditions of high-buffering, the SQS mechanism can convert many times between states 2 and 3 before exiting to either state 1 or 4. By the analysis of Neher and Steinbach (Neher and Steinbach, 1978), states 2 and 3 may be coalesced into a single 'compound' state 2-3, with all rate constants becoming time invariant (Figure S1B). The rate constants in Figure S1B can be understood if we consider the fractional occupancy in state 3 while in compound state '2-3' (Figure S1C):

$$H(t) = \frac{P_3(t)}{P_2(t) + P_3(t)} \approx \begin{cases} H_{\text{high}} = \dfrac{k_{\text{on}} \cdot Ca_{\text{spike}}^2}{k_{\text{on}} \cdot Ca_{\text{spike}}^2 + k_{\text{off}}} \approx 1 & \text{when channel is open} \\ \\ H_{\text{low}} = \qquad 0 & \text{when channel is closed} \end{cases} \qquad (1A\text{-}1)$$

$H(t)$ will fluctuate between H_{high} (during channel openings) and H_{low} (during channel closings). Under high-buffering, $H_{\text{low}} = 0$. Given $Ca_{\text{spike}} \sim 100 \ \mu M$ (Neher, 1998) and typical k_{on} and k_{off} of a lobe of CaM (Bayley et al., 1984; Martin et al., 1985; Teleman et al., 1986), $H_{\text{high}} \approx 1$. The time-averaged value of $H(t)$, which represents the fraction of time spent in state 3 while within compound state 2-3, thus approximates P_O. Since transitions to state 4 only occur from state 3, the rate constant from state '2-3' to state 4 becomes equal to $\alpha \cdot P_O$. Similarly, the rate constant from state '2-3' to state 1 becomes $a \cdot (1 - P_O)$. Solving this equivalent time-invariant system (Figure S1B) yields the $CDI(\infty)$–P_O relationship reproduced here from main paper Equation 2:

$$CDI(\infty) \ = \ CDI_{\text{max}} \cdot P_{4(SS)} \ = \ CDI_{\text{max}} \cdot \frac{P_O \cdot r}{P_O \cdot (r-1) + 1 + 1/\varepsilon}$$

with individual rate constants (a, b, α, β) defined in Figure S1A, $r = \gamma / \varepsilon$, $\gamma = \alpha / \beta$, and $\varepsilon = a / b$. We add the term CDI_{max} to account for the small open probability of inactivated channels (Imredy and Yue, 1994).

This equation is rather unique, particularly because it can produce $CDI(\infty)$–P_O relations with different curvatures (Figure S1D). To prove this, we can take the first and second derivative with respect to P_O:

$$\frac{\partial}{\partial P_o} CDI(\infty) = CDI_{\text{max}} \cdot \frac{r \cdot \varepsilon \cdot (\varepsilon + 1)}{\left(P_O \cdot \varepsilon \cdot (r-1) + \varepsilon + 1\right)^2} \qquad \frac{\partial^2}{\partial P_o^2} CDI(\infty) = CDI_{\text{max}} \cdot \frac{2 \cdot r \cdot \varepsilon^2 \cdot (\varepsilon + 1) \cdot (1-r)}{\left(P_O \cdot \varepsilon \cdot (r-1) + \varepsilon + 1\right)^3} \qquad \text{(1A-2)}$$

Equation 1A-2 reveals that $CDI(\infty)$ vs. P_O is monotonically increasing (i.e., first derivative > 0). Importantly, if $r > 1$, the second derivative is negative, indicating a saturating $CDI(\infty)$–P_O relation (e.g. red curve in Figure S1D). When $r = 1$, the second derivative is identically zero, indicating a linear $CDI(\infty)$–P_O relationship (gray curve). Finally, when $0 < r < 1$, the second derivative is positive for all P_O, which is synonymous with upward curvature (green curve). As discussed in the main paper, this upward curvature arises from the combination of two measures of protection—slow apoCaM preassociation combined with rapid Ca^{2+} release from CaM. As will be shown, the SQS mechanism is uniquely distinguished by this upward curvature among a large class of alternate mechanisms.

1B. The SQS mechanism cannot exhibit upward curvature without an apoCaM binding site

If the apoCaM binding site is absent, $\varepsilon = 0$. The analytic solution in this case can be found by multiplying the numerator and denominator of main paper Equation 2 by ε/γ, and setting $\varepsilon = 0$.

$$CDI(\infty) = \underbrace{CDI_{\text{max}}}_{G} \cdot \frac{P_O}{P_O + \underbrace{1/\gamma}_{k_{\text{eff}}}} = \ G \cdot \frac{P_O}{P_O + k_{\text{eff}}} \qquad \text{(1B-1)}$$

We can take the first and second derivative with respect to P_O:

$$\frac{\partial}{\partial P_o} CDI(\infty) = G \cdot \frac{K_{\text{eff}}}{\left(P_O + K_{\text{eff}}\right)^2} > 0 \qquad \frac{\partial^2}{\partial P_o^2} CDI(\infty) = -G \cdot \frac{2K_{\text{eff}}}{\left(P_O + K_{\text{eff}}\right)^3} < 0 \qquad \text{(1B-2)}$$

The $CDI(\infty)$–P_O relationship in the absence of apoCaM binding is of a Michaelis-Menton form. For this form, the first derivative is always positive, which states that CDI increases with increasing P_O. The second derivative is always negative, which formally establishes that the curvature must always be saturating in nature. Thus, complete removal of the first measure of protection (i.e. apoCaM protection)

precludes global $CDI(\infty)$–P_O relationships with upward curvature.

1C. A 'quick-quick-slow' (QQS) mechanism cannot exhibit upward curvature

Section 1B proves that apoCaM binding is required for upward curvature. Here, we prove that upward curvature only arises when apoCaM binding is slow, as in the SQS mechanism. As a counterexample, suppose apoCaM binding is 'quick,' as would be the case in a QQS mechanism (Figure S2A). Here, the system may convert many times between states 1, 2 and 3 before exiting to state 4. By the analysis of Neher and Steinbach (Neher and Steinbach, 1978), states 1, 2 and 3 may be coalesced into a single 'compound' state 1-2-3, with all rate constants becoming time invariant (Figure S2B).
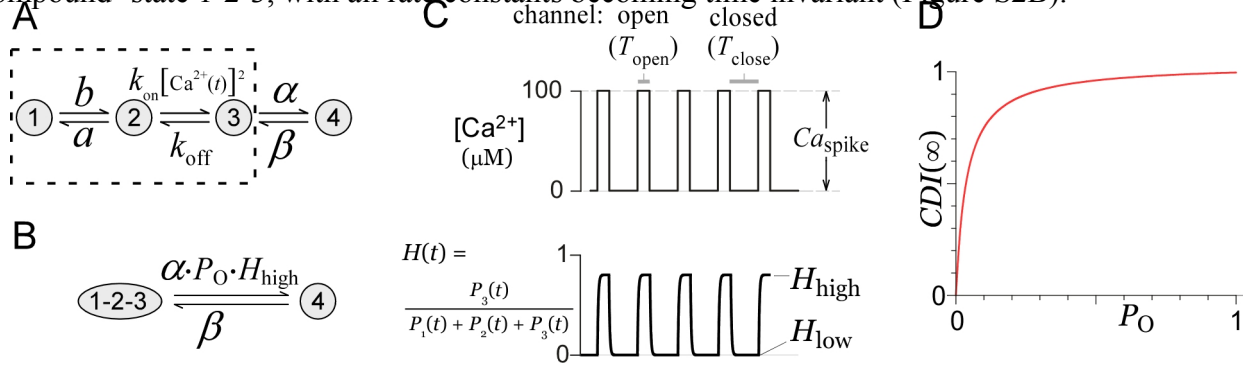
Figure S2 Analytic solution of the QQS mechanism. (A) Basic time-varying 4-state model. (B) Equivalent time-invariant QQS model. (C) Schematized Ca^{2+} signal under high buffering (top) and corresponding oscillations of fractional state 3 occupancy (bottom). (D) Steady-state QQS behavior, plotted according to Equation 1C-2 with $G = 1$ and $K_{eff} = 0.025$.

The fractional occupancy in state 3 while in compound state 1-2-3 (Figure S1C) becomes:

$$H(t) = \frac{P_3(t)}{P_1(t) + P_2(t) + P_3(t)} \approx \begin{cases} H_{high} = \dfrac{1}{1 + (1+\varepsilon)\cdot k_{off}/(k_{on}\cdot Ca_{spike}^2)} & \text{channel open} \\[2em] H_{low} = \qquad\qquad\text{o} & \text{channel closed} \end{cases} \qquad (1C\text{-}1)$$

Under high-buffering, $H(t)$ will fluctuate between H_{high} (during channel openings) and $H_{low} = 0$ (during channel closings). The time-averaged value of $H(t)$ represents the fraction of time spent in state 3 while within compound state 1-2-3. The average $H(t)$ thus approximates $P_O \cdot H_{high}$. Since transitions to state 4 only occur from state 3, the rate constant from the compound state to state 4 becomes equal to $\alpha \cdot P_O \cdot H_{high}$ (Figure S2B). Solving this equivalent time-invariant system yields the $CDI(\infty)$–P_O relationship:

$$CDI(\infty) = \underbrace{CDI_{max}}_{G} \cdot \frac{P_O}{P_O + \underbrace{1/(\gamma \cdot H_{high})}_{K_{eff}}} = G \cdot \frac{P_O}{P_O + K_{eff}} \qquad (1C\text{-}2)$$

Even though CaM kinetics are rapid in this case, the result is of a Michaelis-Menton form. By the analysis of Equation 1B-2, the QQS regime will always produce saturating $CDI(\infty)$–P_O relations inconsistent with global Ca^{2+} selectivity. This can be understood as follows. In the SQS mechanism, the first protective measure is effective because the duration of state 1 occupancy outlasts the duration of channel openings. In the QQS regime, however, state 1 occupancy is brief, thus undermining its protective nature. The resulting system behaves as if it were lacking apoCaM preassociation (compare Equations 1C-2 and 1B-1).

1D. A slow CaM mechanism cannot exhibit upward curvature

The slow-CaM analytic solution is reproduced here from main paper, Equation 1:

$$CDI(\infty) = G \cdot \frac{P_O}{P_O + K_{eff}}$$

Details of the derivation of this equation appear in Supplementary Information 2. Given this result, we can appreciate that this also conforms to a Michaelis-Menton form, consistent only with saturating curvature (via the analysis of Equation 1B-2). Thus, removing the second measure of protection (i.e. rapid Ca^{2+} release from CaM) precludes global $CDI(\infty)$–P_O relationships with upward curvature.

1E. Relaxing kinetic constraints of the SQS mechanism diminishes $CDI(\infty)$–P_O upward curvature.

Thus far, we have proven that the SQS mechanism is capable of producing upward curvature (Section 1A), and that mechanisms with large deviations from the SQS regime cannot produce upward curvature (Sections 1B-1D). Here we explore the uniqueness of the SQS mechanism further, and demonstrate that even subtle deviations from the SQS mechanism (e.g., moderately speeding state 1-2 transitions, slowing state 2-3 transitions, and other kinetic adjustments) will always produce $CDI(\infty)$–P_O relations residing above the prototypic curve for a given r in main paper Equation 2. Hence, upward curvature can only arise from the basic four-state system (main paper Figure 2A) insofar as the SQS mechanism is approximated.

To facilitate these proofs, we first derive an analog to main paper Equation 2, which holds for all regimes of CaM kinetics. Consider the general time-varying system in main paper Figure 2A (or Figure S1A). We can determine several concrete statements about the time averages of occupying various states. For example, we define the time average of occupying state 3 as

$$\langle P_3(t) \rangle = \lim_{T \to \infty} \frac{1}{T} \int_{t=0}^{T} P_3(t)\, dt \tag{1E-1}$$

We also find it convenient to define

$$\langle H(t) \rangle = \frac{\langle P_3(t) \rangle}{\langle P_2(t) \rangle + \langle P_3(t) \rangle} \tag{1E-2}$$

Over time, with a recurring pattern of Ca^{2+} influx, the net flux across any transition must be zero. Thus:

$$\langle P_3(t) \rangle \cdot \alpha = \langle P_4(t) \rangle \cdot \beta \tag{1E-3}$$

$$\langle P_1(t) \rangle \cdot b = \langle P_2(t) \rangle \cdot a \tag{1E-4}$$

Finally, by the definition of probability, it must be that

$$\langle P_1(t) \rangle + \langle P_2(t) \rangle + \langle P_3(t) \rangle + \langle P_4(t) \rangle = 1 \tag{1E-5}$$

Equations 1E-2 through 1E-5 are a set of four equations, with four unknowns ($\langle P_1(t) \rangle$ through $\langle P_4(t) \rangle$). Recalling that $CDI(\infty) = CDI_{max} \cdot \langle P_4(t) \rangle$, algebraic manipulation yields a rather amazing result:

$$CDI(\infty) = CDI_{max} \cdot \frac{\langle H(t) \rangle \cdot r}{\langle H(t) \rangle \cdot (r-1) + 1 + 1/\varepsilon} \tag{1E-6}$$

This equation is entirely analogous to main paper Equation 2, except that P_O is replaced by $\langle H(t) \rangle$. Hence, the intuitive power and mechanistic insight of main paper Equation 2 is incorporated within Equation 1E-6.

The key advantage to Equation 1E-6, however, is that it *always* holds true, even when the kinetics of CaM are not fast, and when the kinetics of state 1-2 or state 3-4 transitions are not slow.

Armed with this general theoretical result (Equation 1E-6), we can sketch proofs that the $CDI(\infty)$–P_O relations for systems that deviate from the SQS mechanism will always reside above those predicted by main paper Equation 2, for a given value of r. A good place to start is to consider how $\langle H(t) \rangle$ relates to P_O. For the case of the SQS mechanism, with rapid CaM kinetics under high buffering (as in Figure S1), $\langle H(t) \rangle = P_O$ (Figure S3A, solid line). Feeding this identity relation through Equation 1E-6 thereby produces main paper Equation 2, with $CDI(\infty)$–P_O relations shown as solid curves in Figure S3B.

What if the kinetics of CaM slow down? As an illustrative example, we consider a system in which the kinetics of Ca^{2+} (un)binding from CaM are somewhat slow compared to T_{close}. We also maintain that transitions between states 1 and 2 remain slow, as well as those between states 3 and 4. Given these latter regimes, we could simulate the behavior of $\langle H(t) \rangle$, based solely on a subsystem containing states 2 and 3. Numerical simulations were performed to calculate $\langle H(t) \rangle$, with $k_{on} \cdot Ca^2_{spike} = 1 \times 10^2 \ ms^{-1}$, $k_{off} = 2 \ ms^{-1}$, $T_{open} = 1$ ms, and T_{close} was varied to adjust P_O ($= T_{open} / (T_{open} + T_{close})$) between zero and unity. The results of the simulation are shown as the dashed curve in Figure S3A. Importantly, the dashed curve resides *above* the line of identity. Thus, feeding the dashed relation in Figure S3A through Equation 1E-6 produces the dashed curves in the $CDI(\infty)$–P_O graph (Figure S3B). Additional simulations illustrate that further slowing of k_{off} enhances the degree to which these curves are shifted upwards (Figure S3A), whereas lesser slowing of k_{off} has the opposite effect.
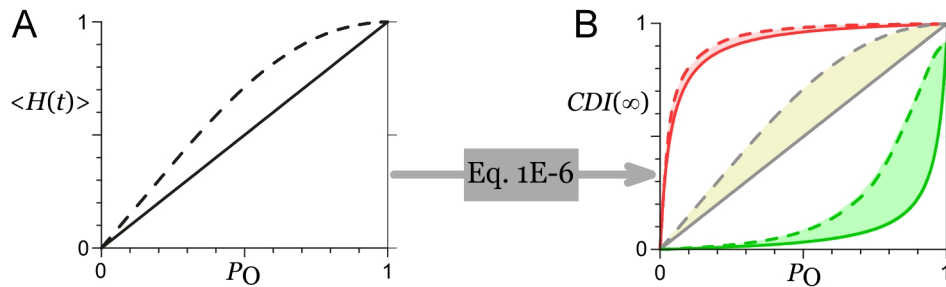
Figure S3. Generalized theory for kinetic deviations from SQS regime. (A) Transformation from P_O to $\langle H(t) \rangle$. For the SQS mechanism, the relation is the line of identity. Deviations from SQS (e.g., slowing of CaM) cause $\langle H(t) \rangle$-P_O relations to deviate upwards, as shown by the dashed curve. (B) Resulting $CDI(\infty)$–P_O curves, obtained by mapping panel A through Equation 1E-6. Solid line in panel A yields solid curves in panel B. Dashed lines in panel A yield dashed curves in panel B.

These numerical results can be supported more generally by solving explicitly for the analytic solution to a subsystem comprised of states 1-3. State 4 can be considered separately because exchange between states 3 and 4 are slow, in accord with the typical kinetics of CDI onset and recovery (Schnee and Ricci, 2003). The bi-exponential solution for the subsystem would provide the analytic relation between P_O and $\langle H(t) \rangle$, confirming that whenever the kinetic constraints of the SQS mechanism are relaxed, the corresponding relation in the $\langle H(t) \rangle$–P_O plane (Figure S3A) will always reside *above* the identity relation. Hence, upon transformation through Equation 1E-6, the corresponding $CDI(\infty)$–P_O curves will always reside *above* the curves predicted by the SQS mechanism (main paper Equation 2).

In sum, for extreme deviations from the SQS regime, the resulting mechanisms (e.g., slow CaM or QQS) produce Michaelis-Menton $CDI(\infty)$–P_O relations, incapable of upward curvature (Sections 1B-1D). Mechanisms with subtler deviations from the SQS regime always experience a reduced ability to realize the

global end of the spectrum (Figure S3B, green shaded area is lost). Hence, global $CDI(\infty)$–P_O relations can only arise from the basic four-state system insofar as the SQS mechanism is approximated.

1F. Disfavored states reduce the upward curvature of SQS-mechanism $CDI(\infty)$–P_O relations.
Beyond simply changing the relative kinetics of rate constants within the SQS mechanism, what would happen if additional disfavored states were added? The main text contends that a basic four-state mechanism embodies the dominant conformations of the CaM/channel complex. Direct Ca^{2+} binding to preassociated apoCaM, which would create an additional state 5 (Figure S4A), was omitted, given that such interaction appears unlikely in an analogous apoCaM/peptide atomic structure (Houdusse et al., 2006). ApoCaM binding to the effector site, which would generate an additional state 6 (Figure S4A), was also left out, because CDI is absent without Ca^{2+}. Here, we consider the effects of including these additional states, and find that their inclusion diminishes the degree to which $CDI(\infty)$–P_O relations with upward curvature can be produced. This analysis strengthens the case for omitting these disfavored states, since their presence would contradict the experimentally quantified upward curvature of N-lobe regulation.
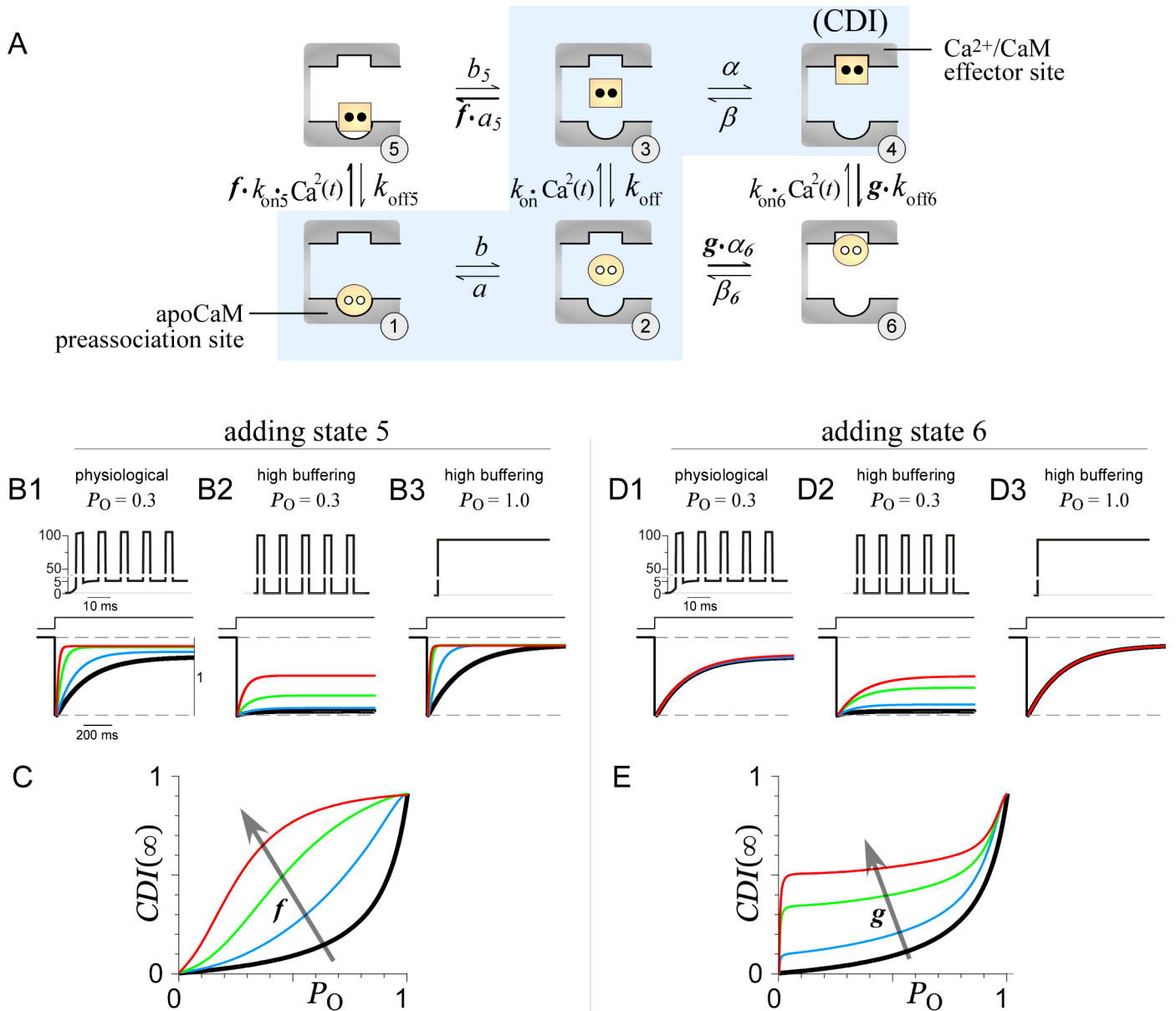
Figure S4. Inclusion of disfavored states diminishes $CDI(\infty)$–P_O upward curvature. (A) General six-state configuration with original four states in shaded region. Disfavored states include Ca^{2+}-CaM bound to apoCaM site (state 5), and apoCaM bound to Ca^{2+}/CaM site (state 6). Rate constants interconnecting states 1-4 have the original N-lobe values (main text Figure 2G). Additional parameters: for state 5, $a_5 = 0.003$ ms^{-1}, $b_5 = 1$ ms^{-1}, $k_{on5} = 1.1\times10^6$ M^{-2} ms^{-1}, and $k_{off5} = 0.03$ ms^{-1}; for state 6, $\alpha_6 = 0.1$ ms^{-1}, $\beta_6 = 0.01$ ms^{-1}, $k_{on6} = 3.7\times10^8$ M^{-2} ms^{-1}, and $k_{off6} = 0.0003$ ms^{-1}. Scaling factor f is applied to a_5 and k_{on5}; scaling factor g is applied to α_6 and k_{off6}. (B-C) Progressive addition of state 5 ($f = 1$, blue; 6.7, green; and 33.3, red), while state 6 is omitted ($g = 0$). Baseline 4-state ($f = 0$, $g = 0$) in black. Format as in main text Figure 2G-H. (D-E) Progressive addition of state 6 ($g = 1$, blue; 5, green; and 10, red), while state 5 is omitted ($f = 0$). See Supplementary Information 4F for detailed numerical simulation methods.

Figure S4A diagrams a generalized set of CaM/channel conformations, where the original four states appear within the shaded region. Additionally, the new scheme includes Ca^{2+}-bound CaM associated with the apoCaM preassociation site (state 5), as well as apoCaM bound to the Ca^{2+}/CaM effector site (state 6). To accord with the lack of CDI in the absence of Ca^{2+}, state 6 does not produce CDI. The effects of including states 5 or 6 are illustrated by numerical simulations (Figure S4, B-E). In these computations, all rate constants directly interconnecting the standard SQS states (1, 2, 3, 4) were held at their original values, as given in the main text (Figure 2G). The additional parameters of the six-state model are detailed in the figure legend of Figure S4. Because these parameters must accord with thermodynamic detailed balance, only six of the eight parameters could be freely modified. For convenience, we introduce two scale factors, f and g, which can be adjusted to induce occupancy of states 5 and 6 in a graded manner, while respecting thermodynamic constraints (Figure S4A).

Figure S4B-C explores the effects of including state 5. For orientation, black traces reproduce the baseline behavior of the four-state SQS mechanism (i.e., $f = 0$ and $g = 0$), as presented in the main text (Figure 2G-H, with $r = 1/10$). For the colored traces, we preclude state 6 occupancy ($g = 0$) and introduce state 5 occupancy in a graded manner ($f = 1$, blue; 6.7, green; and 33.3, red). Interestingly, CDI for every Ca^{2+} input is enhanced (Figure S4B) compared to the usual SQS behavior, and the degree of enhancement is proportional to f. Importantly, state 5 occupancy induces CDI in response to intermittent local Ca^{2+} signals (Figure S4B2). This inability to reject local Ca^{2+} signals corresponds to $CDI(\infty)$–P_O relations with diminishing upward curvature (Figure S4C), and diminished global Ca^{2+} selectivity. Intuitively, this outcome is expected because allowing state 5 occupancy (i.e. allowing state 1 to directly bind Ca^{2+}) undermines the extent to which preassociated apoCaM is sheltered from large Ca^{2+} spikes, thus weakening the first of two 'measures of protection.'
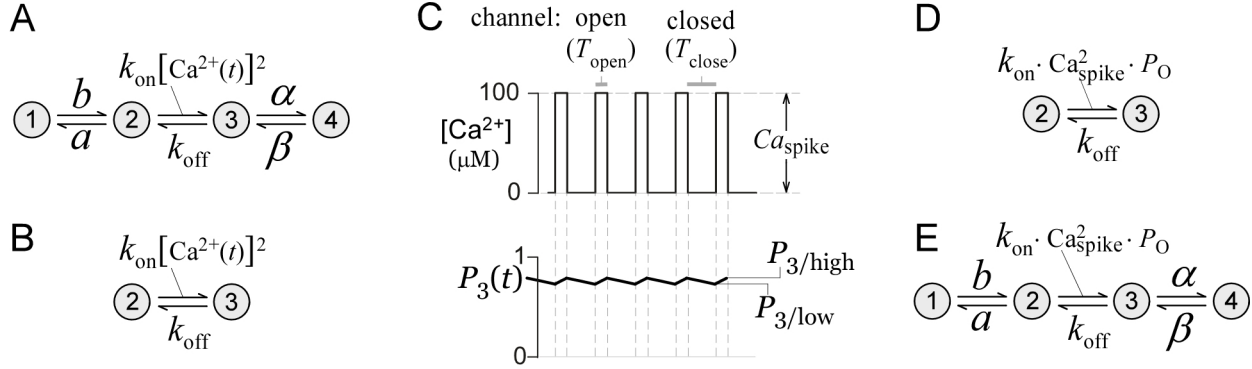
Figures S4D-E summarize a similar analysis regarding occupancy of state 6. The behavior of the four-state SQS mechanism is again displayed for reference in black. Here, we preclude state 5 occupancy ($f = 0$) and introduce state 6 occupancy in a graded manner ($g = 1$, blue; 5, green; and 10, red). In this case, CDI in response to a global pedestal (Figure S4D1) or continuously present local Ca^{2+} signal (Figure S4D3) are unaffected by inclusion of state 6. However, CDI in response to intermittent Ca^{2+} spikes (Figure S4D2) grows with increasing state 6 occupancy, resulting in progressively diminishing upward curvature in $CDI(\infty)$–P_O relations (Figure S4E), and diminished global Ca^{2+} selectivity. This finding accords with intuition because state 6 competes with state 1 for apoCaM. Thus, some fraction of apoCaM will reside in state 6, wherein CaM is unprotected from large Ca^{2+} spikes.

In summary, this section argues that the SQS mechanism is rather unique in its ability to support global Ca^{2+} selectivity, as visualized by $CDI(\infty)$–P_O relations with upward curvature. Any generic mechanism (Figure S4A) which manages to produce global selectivity only does so to the degree that the SQS mechanism is approximated. For this reason, and the close correspondence of main text Equation 2 with experimentally determined $CDI(\infty)$–P_O relations, we favor the essential four-state SQS mechanism.

2. Supplemental Slow CaM Theory

2A. Simplifications of the CaM decoding mechanism when CaM kinetics are slow

This section proves that when the kinetics of Ca^{2+} binding to or unbinding from a lobe of CaM are slow, the steady-state behavior of the time-varying system in Figure S5A (equivalent to main paper Figure 2A) can be well-approximated by the simpler system in Figure S5E (equivalent to main paper Figure 2E). In this alternate system, the rate constant for transition from state 2 to 3 is not treated as pulsating with fluctuating Ca^{2+}, but is held constant at $k_{on} \cdot Ca^2_{spike} \cdot P_O$. Before dissecting the system, we specifically define 'slow CaM kinetics' by the condition $k_{on} \cdot Ca^2_{spike} + k_{off} \ll 1/T_{open}$ or $k_{off} \ll 1/T_{close}$.

A

$$\textcircled{1} \underset{a}{\overset{b}{\rightleftarrows}} \textcircled{2} \underset{k_{off}}{\overset{k_{on}[Ca^{2+}(t)]^2}{\rightleftarrows}} \textcircled{3} \underset{\beta}{\overset{\alpha}{\rightleftarrows}} \textcircled{4}$$

B

$$\textcircled{2} \underset{k_{off}}{\overset{k_{on}[Ca^{2+}(t)]^2}{\rightleftarrows}} \textcircled{3}$$

C channel: open (T_{open}) closed (T_{close})

D

$$\textcircled{2} \underset{k_{off}}{\overset{k_{on} \cdot Ca^2_{spike} \cdot P_O}{\rightleftarrows}} \textcircled{3}$$

E

$$\textcircled{1} \underset{a}{\overset{b}{\rightleftarrows}} \textcircled{2} \underset{k_{off}}{\overset{k_{on} \cdot Ca^2_{spike} \cdot P_O}{\rightleftarrows}} \textcircled{3} \underset{\beta}{\overset{\alpha}{\rightleftarrows}} \textcircled{4}$$

Figure S5. Analytic solution of the slow CaM mechanism. (A) Basic time-varying 4-state model. (B) Excised portion of time-varying model. (C) Schematized Ca^{2+} signal under high buffering (top) and corresponding steady-state oscillations of state 3 occupancy for panel B model (bottom). (D) Equivalent model to that in panel B, under conditions of slow CaM. (E) Equivalent model to that in panel A, under conditions of slow CaM.

To start, we consider a portion of the complete time-varying system, in which states 2 and 3 are excised (Figure S5B). If this subsystem is continuously driven by a Ca^{2+} spike train (high Ca^{2+} buffering conditions), as shown in Figure S5C (top), the subsystem will eventually achieve an exactly recurring pattern of oscillations in state 3 probability $P_3(t)$ (Figure S5C, bottom). At steady-state, $P_3(t)$ at the end of channel open and closed periods can be solved explicitly:

$$P_{3/high} = P_{3/low} \cdot e^{-u} + P_{3\infty} \cdot (1 - e^{-u}) \quad and \quad P_{3/low} = P_{3/high} \cdot e^{-d} \tag{2A-1}$$

where $P_{3\infty} = k_{on} \cdot Ca^2_{spike} / (k_{on} \cdot Ca^2_{spike} + k_{off})$, $u = T_{open}(k_{on} \cdot Ca^2_{spike} + k_{off})$, and $d = T_{close} \cdot k_{off}$. Note that $P_{3\infty}$ represents the probability of populating state 3 if Ca_{spike} were to persist indefinitely, and adopts values within the range 0 to 1. The relative speed of CaM kinetics as compared to channel opening/closing durations are represented by u and d, which are unitless positive real numbers. We can think of u as a measure of the upward deflection in $P_3(t)$ during channel openings, and d as a measure of its downward deflection during channel closings (Figure S5C, bottom). If Ca^{2+} binding is slow relative to channel openings, then $u \ll 1$, and the upward deflections in $P_3(t)$ are minimal. If Ca^{2+} release is slow relative to channel closings, then $d \ll 1$, and the downward deflections in $P_3(t)$ are minimal. Solving the system of two equations (Equation 2A-1) yields:

$$P_{3/high} = P_{3\infty} \cdot \frac{e^{u+d} - e^d}{e^{u+d} - 1} \quad and \quad P_{3/low} = P_{3\infty} \cdot \frac{e^u - 1}{e^{u+d} - 1} \tag{2A-2}$$

First, suppose that both $u \ll 1$ and $d \ll 1$, that is, $k_{on} \cdot Ca^2_{spike} + k_{off} \ll 1/T_{open}$ and $k_{off} \ll 1/T_{close.}$ In this case, $e^u \approx u + 1$ and $e^d \approx d + 1$. The equations in (2A-2) can then be simplified as follows:

$$P_{3/high} \sim P_{3/low} \sim P_{3(SS)} = P_{3\infty} \frac{u}{u+d} = \frac{k_{on} \cdot Ca^2_{spike} \cdot P_O}{(k_{on} \cdot Ca^2_{spike} \cdot P_O + k_{off})} \qquad (2A-3)$$

where the channel open probability $P_O = T_{open} / (T_{open} + T_{close})$. Two points merit emphasis. First, Equation 2A-3 states that the occupancy of state 3 essentially does not change between channel openings and closings, thus the behavior of the system is non-pulsatile. Second, Equation 2A-3 is exactly the steady-state solution that would be predicted by the subsystem in Figure S5D, where the rate constant for transition from state 2 to 3 is time invariant and equal to $k_{on} \cdot Ca^2_{spike} \cdot P_O$. Hence, the time-varying subsystem in Figure S5B is well approximated by the time-invariant subsystem in Figure S5D.

In actuality, the C-lobe of CaM is unlikely to satisfy both conditions that $u \ll 1$ and $d \ll 1$. Based on typical k_{off} for the C-lobe (Bayley et al., 1984; Martin et al., 1985; Teleman et al., 1986), it is clear that $d \ll 1$ (i.e. $k_{off} \ll 1/T_{close}$ for slow Ca^{2+} release). However, given best estimates for $Ca_{spike} \sim 100$ μM (Neher, 1998), $k_{on} \cdot Ca^2_{spike}$ is likely much greater than $1/T_{open}$, i.e. $u \gg 1$ (fast Ca^{2+} binding). Nonetheless, the approximation made in Figure S5D and Equation 2A-3 will still hold when either $u \ll 1$ or $d \ll 1$.
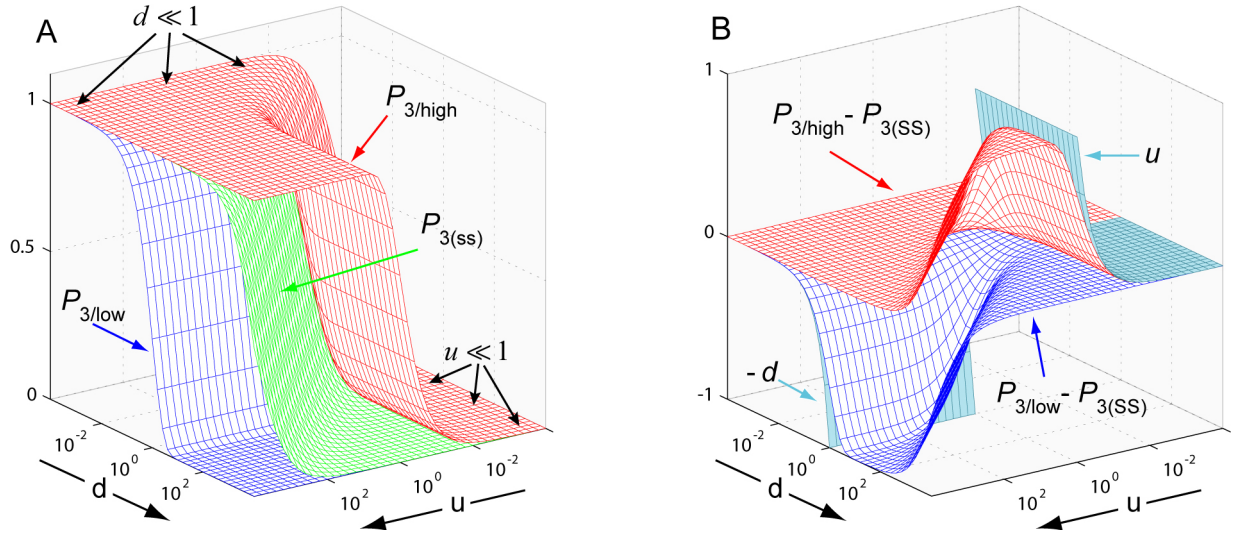
Figure S6 Behavior of the time-varying 2-state model (Figure S5B), under conditions of high-buffering, as in Figure S5C. (A) Numerical values of $P_{3/high}$ (red), $P_{3/low}$ (blue), and $P_{3(SS)}$ (green), from Equation 2A-2 and Equation 2A-3. Here we assume that spike Ca^{2+} is large, and thus $P_{3\infty}=1$. (B) Deviations from $P_{3(SS)}$ of $P_{3/high}$ (red) and $P_{3/low}$ (blue). Across all values of u and d, the maximal deviation from $P_{3(SS)}$ is bounded by $min(u,d)$ (cyan surface), demonstrating Equation 2A-4.

In Figure S6A, we show numerical values of $P_{3/high}$ (red) and $P_{3/low}$ (blue) from Equation 2A-2, and of $P_{3(SS)}$ (green) from Equation 2A-3. As can be seen, the simplification of Figure S5D (i.e. that the system is non-pulsatile) is actually true when either $u \ll 1$ or $d \ll 1$. This is further appreciated if we look at the residuals between the fluctuations in $P_3(t)$ and $P_{3(SS)}$ (Figure S6B): $P_{3/high} - P_{3(SS)}$ (red) and $P_{3/low} - P_{3(SS)}$ (blue) are both very close to zero (i.e. system is non-pulsatile) when either $u \ll 1$ or $d \ll 1$. The system only becomes pulsatile when both $u \gg 1$ and $d \gg 1$ (which is a requirement for the SQS regime). It can rigorously be shown that the maximum deviation of $P_3(t)$ from $P_{3(SS)}$ is bounded by the minimum of u and d. i.e.:

$$max\left(\left|P_3(t) - P_{3(SS)}\right|\right) \leq P_{3\infty} \cdot min(u,d) \leq min(u,d) \qquad (2A-4)$$

Equation 2A-4 gives a very important result: when either $u \ll 1$ or $d \ll 1$ (i.e. slow CaM), the oscillations in $P_3(t)$ must also be small (as in Figure S5C, bottom), and $P_3(t)$ is closely approximated by $P_{3(SS)}$. The proof of Equation 2A-4 rests on the following four claims, for which it is helpful to refer to Figure S6B:

1. $P_{3/high} - P_{3(ss)} > 0$ and $P_{3(ss)} - P_{3/low} > 0$

2. If $d \geq u$, then $P_{3/high} - P_{3(ss)} \geq P_{3(ss)} - P_{3/low}$;   If $u \geq d$, then $P_{3(ss)} - P_{3/low} \geq P_{3/high} - P_{3(ss)}$. Thus:

$$max\left| P_3(t) - P_{3(SS)} \right| = \begin{cases} P_{3/high} - P_{3(SS)} & \textit{iff } d \geq u \\ P_{3(SS)} - P_{3/low} & \textit{iff } u \geq d \end{cases}$$

3. The derivative of $(P_{3/high} - P_{3(ss)})$ with respect to d is always positive, thus, $max(P_{3/high} - P_{3(ss)})$ for any fixed u occurs at $d \to +\infty$. Plugging in $d \to +\infty$ and simplifying yields: $max(P_{3/high} - P_{3(ss)}) \leq P_{3\infty} \cdot u$. Combining this result with claim #2, we satisfy Equation 2A-4 when $d \geq u$.

4. The derivative of $(P_{3(ss)} - P_{3/low})$ with respect to u is always positive; thus, $max(P_{3(ss)} - P_{3/low})$ for any fixed d occurs at $u \to +\infty$. Plugging in $u \to +\infty$ and simplifying yields: $max(P_{3(ss)} - P_{3/low}) \leq P_{3\infty} \cdot d$. Combining this result with claim #2, we satisfy Equation 2A-4 when $u \geq d$.

The algebra involved in proving these claims is lengthy, and for brevity they are here omitted. It can be appreciated in Figure S6B that each claim is rigorously true.

To summarize, Equation 2A-4 states that when CaM is slow (either $u \ll 1$ or $d \ll 1$, equivalently, $k_{on} \cdot Ca_{spike}^2 + k_{off} \ll 1/T_{open}$ or $k_{off} \ll 1/T_{close}$), the subsystem in Figure S5B reaches a non-pulsatile steady state, approximated by the simpler mechanism in Figure S5D. In terms of differential equations, this result is equivalent to the statement

$$\frac{dP_2(t)}{dt} = \overbrace{-k_{on} \cdot [Ca(t)]^2 \cdot P_2(t) + k_{off} \cdot P_3(t)}^{\text{term } x} \sim 0$$

$$\frac{dP_3(t)}{dt} = \underbrace{+k_{on} \cdot [Ca(t)]^2 \cdot P_2(t) - k_{off} \cdot P_3(t)}_{-\text{term } x} \sim 0$$

(2A-5)

Now we turn to the full time-varying system in Figure S5A. The complete set of differential equations for this system is

$$\frac{dP_1(t)}{dt} = \overbrace{-b \cdot P_1(t) + a \cdot P_2(t)}^{\text{term } y}$$

$$\frac{dP_2(t)}{dt} = \overbrace{+b \cdot P_1(t) - a \cdot P_2(t)}^{-\text{term } y} \underbrace{-k_{on} \cdot [Ca(t)]^2 \cdot P_2(t) + k_{off} \cdot P_3(t)}_{\text{term } x}$$

$$\frac{dP_3(t)}{dt} = \underbrace{+k_{on} \cdot [Ca(t)]^2 \cdot P_2(t) - k_{off} \cdot P_3(t)}_{-\text{term } x} \overbrace{-\alpha \cdot P_3(t) + \beta \cdot P_4(t)}^{\text{term } z}$$

$$\frac{dP_4(t)}{dt} = \overbrace{+\alpha \cdot P_3(t) - \beta \cdot P_4(t)}^{-\text{term } z}$$

(2A-6)

with the fluctuating Ca^{2+} inputs as shown in Figure S5C. Since the solution to these equations is unique, any solution that satisfies the equations must be *the* solution. We therefore may utilize an educated guess, based heavily on the simplified system (Figure S5E), to derive the final solution under conditions of slow CaM kinetics. The guess is as follows.

$$P_1(t) = P_{1(SS)} = \frac{\varepsilon \cdot (1 - H_{SS})}{1 + \varepsilon + (\gamma - \varepsilon) \cdot H_{SS}}$$

$$P_2(t) = P_{2(SS)} = \frac{(1 - H_{SS})}{1 + \varepsilon + (\gamma - \varepsilon) \cdot H_{SS}}$$

$$P_3(t) = P_{3(SS)} = \frac{H_{SS}}{1 + \varepsilon + (\gamma - \varepsilon) \cdot H_{SS}} \qquad (2A\text{-}7)$$

$$P_4(t) = P_{4(SS)} = \frac{\gamma \cdot H_{SS}}{1 + \varepsilon + (\gamma - \varepsilon) \cdot H_{SS}}$$

$$\text{where } H_{SS} = \frac{k_{on} \cdot Ca_{spike}^2 \cdot P_O}{(k_{on} \cdot Ca_{spike}^2 \cdot P_O + k_{off})}$$

where $\gamma = \alpha / \beta$ (Ca^{2+}/CaM$_{lobe}$ affinity for effector site); and $\varepsilon = a / b$ (apoCaM$_{lobe}$ affinity for preassociation site).

The solution embodied within Equation 2A-7 is equivalent to the steady-state solution for the simplified four-state mechanism in Figure S5E, wherein the rate constant for transition from state 2 to 3 is time invariant and equal to $k_{on} \cdot Ca_{spike}^2 \cdot P_O$. Does this solution satisfy all the constraints in the full system (Equation 2A-6)? If $k_{on} \cdot Ca_{spike}^2 + k_{off} \ll 1/T_{open}$ or $k_{off} \ll 1/T_{close}$, then by Equation 2A-5, term x in Equation 2A-6 is zero. Taking the explicit forms of P_{1SS} and P_{2SS} within Equation 2A-7, and substituting within Equation 2A-6, confirms that term y of Equation 2A-6 is also zero. Finally, taking the explicit forms of P_{3SS} and P_{4SS} within Equation 2A-7, and substituting within Equation 2A-6, confirms that term z of Equation 2A-6 is also zero. Hence, all the time derivatives in Equation 2A-6 are zero, and all elements in our guessed solution (Equation 2A-7) are constants. Moreover, the sum of the probabilities in Equation 2A-7 equals unity. Thus, Equation 2A-7 (Figure S5E) is a valid steady-state solution to the full system in Equation 2A-6 (Figure S5A). Since the solution to this type of mechanism is unique, then Equation 2A-7 represents *the* solution.

To summarize these results:

> If the kinetics of CaM are slow ($k_{on} \cdot Ca_{spike}^2 + k_{off} \ll 1/T_{open}$ or $k_{off} \ll 1/T_{close}$), then the four-state mechanism in Figure S5A (with fluctuating transition rate from state 2 to 3) will reach a non-pulsatile steady-state solution (Equation 2A-7), equivalent to that for a simplified four-state mechanism (Figure S5E), wherein the rate constant for transition from state 2 to 3 is time invariant and equal to $k_{on} \cdot Ca_{spike}^2 \cdot P_O$.

2B. Derivation of main paper Equation 1 (slow CaM analytic equation)

If the Ca^{2+} (un)binding kinetics of CaM are slow, the steady-state extent of CDI can be calculated from the simplified time-invariant system in Figure S5E:

$$CDI(\infty) = CDI_{max} \cdot P_{4(SS)} = CDI_{max} \cdot \underbrace{\left(\frac{\gamma}{1+\gamma}\right)}_{G} \cdot \frac{P_O}{P_O + \underbrace{\left(\frac{1+\varepsilon}{1+\gamma}\right) \cdot \left(\frac{k_{off}}{k_{on} \cdot Ca_{spike}^2}\right)}_{K_{eff}}} = G \cdot \frac{P_O}{P_O + K_{eff}} \qquad (2B\text{-}1)$$

where $\gamma = \alpha/\beta$ (channel effector site affinity for C-lobe in Ca^{2+} bound form); and $\varepsilon = a/b$ (channel preassociation site affinity for C-lobe in Ca^{2+}-free form). We add the term CDI_{max} to account for the small, but potentially non-zero open probability of inactivated channels.

2C. The slow CaM mechanism cannot exhibit buffer sensitivity.

Although the slow CaM derivations (Sections 2A-2B) assumed high-buffering conditions, more broadly, it is possible to solve analytically for $CDI(\infty)$ given arbitrary Ca^{2+} inputs. Based on the derivations in Section 2A, it can be shown that the when the kinetics of Ca^{2+} (un)binding to a lobe of CaM are slow, the time-varying rate constant for transition from state 2 to 3 can be replaced by a time-invariant constant with value $k_{on} \cdot \langle Ca^2(t) \rangle$, where:

$$\langle Ca^2(t) \rangle = \lim_{T \to \infty} \frac{1}{T} \int_{t=0}^{T} Ca^2(t)\, dt \qquad (2C\text{-}1)$$

Essentially, Equation 2C-1 yields the average value of $Ca^2(t)$. Under physiological buffering conditions,

$$\langle Ca^2(t) \rangle = P_O \cdot Ca_{spike}^2 + Ca_{global}^2 \qquad (2C\text{-}2)$$

The resulting time-invariant equivalent system would have a steady-state solution, analogous to Equation 2B-1. Specifically:

$$CDI(\infty) = CDI_{max} \cdot \underbrace{\left(\frac{\gamma}{1+\gamma}\right)}_{G} \cdot \frac{P_O + \left(\frac{Ca_{global}}{Ca_{spike}}\right)^2}{P_O + \left(\frac{Ca_{global}}{Ca_{spike}}\right)^2 + \underbrace{\left(\frac{1+\varepsilon}{1+\gamma}\right) \cdot \left(\frac{k_{off}}{k_{on} \cdot Ca_{spike}^2}\right)}_{K_{eff}}} = G \cdot \frac{P_O + \left(\frac{Ca_{global}}{Ca_{spike}}\right)^2}{P_O + \left(\frac{Ca_{global}}{Ca_{spike}}\right)^2 + K_{eff}} \qquad (2C\text{-}3)$$

If we take $Ca_{global} \sim 5$ μM and $Ca_{spike} \sim 100$ μM (Neher, 1998), then Equation 2C-3 becomes:

$$CDI(\infty) = G \cdot \frac{P_O + 0.0025}{P_O + 0.0025 + K_{eff}} \qquad (2C\text{-}4)$$

Since all of the Ca^{2+}-detection processes of interest exhibit strong CDI under physiological buffering (main paper Figures 1B-C, left), the values of G and K_{eff} can be constrained. Strong $CDI(\infty) \sim 1$ under physiological buffering requires $G \approx 1$, and $K_{eff} \ll 1$. Under conditions of high-buffering, $Ca_{global} = 0$, and Equation 2C-3 reduces to Equation 2B-1. Plugging in $G \approx 1$, and $K_{eff} \ll 1$, it follows that all versions of the slow CaM mechanism which exhibit strong CDI under physiological buffering will invariably produce a nearly equivalent extent of CDI under high buffering. This behavior exemplifies the definition of local selectivity (main paper, Figure 1B).

3. Comparing Continuum and Stochastic Views of Nanodomain Ca^{2+} Signaling and Decoding

Figures 1-2 of the main text convey only the essential features of Ca^{2+} signaling and decoding near the mouth of a Ca^{2+} channel. Local signals are portrayed as step-like waveforms that are hardly affected by strong intracellular Ca^{2+} buffering, as suggested by previous analyses (Neher, 1998; Sherman et al., 1990). Global signals are portrayed as constant-valued signals which are eliminated by the introduction of Ca^{2+} buffering. However, given the small dimensions of a nanodomain (~20 nm hemisphere), an average of only ~1 Ca^{2+} ion would be present during channel openings. Even though this corresponds to a large Ca^{2+} concentration of ~100 μM, the number of nanodomain Ca^{2+} ions would adopt one of several integer values, and thus differ considerably among CaM/channel complexes. This scenario might raise concerns about the accuracy of continuum assumptions. This section validates the simplified view of Ca^{2+} signaling and decoding with in-depth reaction-diffusion modeling. Section 3A discusses possible continuum and stochastic methodologies, which are then implemented in Sections 3B-C. Section 3D verifies that the SQS and slow-CaM decoding mechanisms behave identically whether continuum or stochastic methodologies are employed, and Section 3E offers an intuitive explanation for this identical behavior.

3A. Nanodomain Ca^{2+} signals: setup and possible approaches

This section introduces approaches to solve a reaction-diffusion problem involving a single Ca^{2+} channel and pertinent intracellular Ca^{2+} buffers. The result of such a solution would detail the concentration of free Ca^{2+}, as a function of space and time, near a channel which is gating open and closed. For simplicity, we assume an infinite-half-space geometry, where the plasma membrane is modeled as an infinite planar surface (impermeant to Ca^{2+} and buffers), with a single Ca^{2+} channel acting as a point source for Ca^{2+} entry on the intracellular side. This geometry ensures that the concentration profiles will be hemispherically symmetric. To accord with our experimental internal patch pipette solutions, we consider the case of a single buffer (such as BAPTA), which binds Ca^{2+} according to a first-order kinetic reaction:

$$Ca \;+\; B \; \underset{k_{\text{B,off}}}{\overset{k_{\text{B,on}}}{\rightleftharpoons}} \; CaB \tag{3A-1}$$

Given hemispherical symmetry, the governing reaction-diffusion equations are (Smith, 2001):

$$\frac{\partial\left[Ca^{2+}\right]}{\partial t} = D_{\text{Ca}} \cdot \overbrace{\left(\frac{2}{r_{\text{d}}} \cdot \frac{\partial\left[Ca^{2+}\right]}{\partial r_{\text{d}}} + \frac{\partial^2\left[Ca^{2+}\right]}{\partial r_{\text{d}}^2} \right)}^{\text{diffusion}} \overbrace{- k_{\text{B,on}} \cdot \left[Ca^{2+}\right] \cdot \left[B\right] + k_{\text{B,off}} \cdot \left(B_{\text{T}} - \left[B\right]\right)}^{\text{reaction}} + J$$

$$\frac{\partial\left[B\right]}{\partial t} = D_{\text{B}} \cdot \left(\frac{2}{r_{\text{d}}} \cdot \frac{\partial\left[B\right]}{\partial r_{\text{d}}} + \frac{\partial^2\left[B\right]}{\partial r_{\text{d}}^2} \right) - k_{\text{B,on}} \cdot \left[Ca^{2+}\right] \cdot \left[B\right] + k_{\text{B,off}} \cdot \left(B_{\text{T}} - \left[B\right]\right)$$

$$\tag{3A-2}$$

where each partial derivative with respect to time is the sum of terms describing: diffusion of Ca^{2+} or buffer; reaction of Ca^{2+} and buffer; and introduction of Ca^{2+} (J represents influx of Ca^{2+} from the channel). r_{d} is the distance from the channel in spherical coordinates, not to be confused with the SQS model parameter 'r.' $[Ca^{2+}]$ (free calcium concentration) and $[B]$ (free buffer concentration) are both functions of space and time. D_{Ca} and D_{B} are diffusion coefficients for Ca^{2+} and buffer; $k_{\text{B,on}}$ and $k_{\text{B,off}}$ are the buffer association and dissociation rates. The total buffer concentration, $B_{\text{T}} = [B] + [CaB]$, is presumed constant over all locations on the intracellular side of the membrane. This holds true if the diffusion coefficients of free and bound buffer are equal; a reasonable assumption given the negligible mass of a Ca^{2+} ion compared to a buffer molecule (Stern, 1992). Detailed parameters regarding Equation 3A-2 are in Table S1.

Two sets of boundary conditions also pertain. The first concerns constraints at the channel (Smith, 2001):

$$\lim_{r_{\mathrm{d}}\to 0}\left(2\pi r_{\mathrm{d}}^2 \cdot D_{\mathrm{Ca}} \cdot \frac{\partial\left[Ca^{2+}\right]}{\partial r_{\mathrm{d}}}\right) = \frac{i_{\mathrm{Ca}}}{2\cdot F} \qquad \lim_{r_{\mathrm{d}}\to 0}\left(2\pi r_{\mathrm{d}}^2 \cdot D_{\mathrm{B}} \cdot \frac{\partial\left[B\right]}{\partial r_{\mathrm{d}}}\right) = 0 \qquad (3A\text{-}3)$$

where i_{Ca} is the unitary current, and F is Faraday's constant. Equation 3A-3 stipulates that at $r_{\mathrm{d}} = 0$, the diffusion terms of Equation 3A-2 go to zero, and the influx term (J) of Equation 3A-2 behaves as a point source of Ca^{2+} ions, located at $r_{\mathrm{d}} = 0$, with current i_{Ca}.

The second set of boundary conditions relates to constraints at an infinite distance from the channel, where only global Ca^{2+} signals are present.

$$\lim_{r_{\mathrm{d}}\to\infty}\left[Ca^{2+}\right] = Ca_{\mathrm{global}} = \frac{k_{\mathrm{B,on}}\left(Ca_{\mathrm{T}\infty} - B_{\mathrm{T}}\right) - k_{\mathrm{B,off}} + \sqrt{k_{\mathrm{B,on}}^2\left(Ca_{\mathrm{T}\infty} - B_{\mathrm{T}}\right)^2 + 2k_{\mathrm{B,on}}k_{\mathrm{B,off}}\left(Ca_{\mathrm{T}\infty} + B_{\mathrm{T}}\right) + k_{\mathrm{B,off}}^2}}{2k_{\mathrm{B,on}}}$$

$$(3A\text{-}4)$$

$$\lim_{r_{\mathrm{d}}\to\infty}\left[B\right] = B_{\mathrm{global}} = \frac{-k_{\mathrm{B,on}}\left(Ca_{\mathrm{T}\infty} - B_{\mathrm{T}}\right) - k_{\mathrm{B,off}} + \sqrt{k_{\mathrm{B,on}}^2\left(Ca_{\mathrm{T}\infty} - B_{\mathrm{T}}\right)^2 + 2k_{\mathrm{B,on}}k_{\mathrm{B,off}}\left(Ca_{\mathrm{T}\infty} + B_{\mathrm{T}}\right) + k_{\mathrm{B,off}}^2}}{2k_{\mathrm{B,on}}}$$

Ca_{global} and B_{global} are the steady-state concentrations of free Ca^{2+} and free buffer in the bulk of the cytosol ($r_{\mathrm{d}} \to \infty$). Note that the total buffer concentration, $B_{\mathrm{T}} = [B] + [CaB]$, is fixed regardless of proximity to the channel. By contrast, because there is a point-source of Ca^{2+} at $r_{\mathrm{d}} = 0$, the total Ca^{2+} concentration is higher when closer to the channel. Because of this, Equation 3A-4 utilizes a new parameter that describes the total Ca^{2+} concentration very far from the channel: $Ca_{\mathrm{T}\infty} = \lim_{r_{\mathrm{d}}\to\infty}\left(\left[Ca^{2+}\right] + \left[CaB\right]\right)$. $Ca_{\mathrm{T}\infty}$ can be thought of as the bulk Ca^{2+} load. The balance between $Ca_{\mathrm{T}\infty}$ and B_{T} determines the bulk free Ca^{2+} concentration, Ca_{global}.

By examining Equation 3A-4, it can be seen that if $B_{\mathrm{T}} = 0$, $Ca_{\mathrm{global}} = Ca_{\mathrm{T}\infty}$. Thus, under zero-buffer conditions, a global Ca^{2+} signal of ~5 µM can be readily achieved. By contrast, under conditions of 10 mM BAPTA, $B_{\mathrm{T}} = 10{,}000$ µM, resulting in Ca_{global} ~0 (Table S1). This confirms that high buffering eliminates the global Ca^{2+} signal.

		No buffer	10 mM BAPTA
buffer conditions	$k_{\mathrm{B,on}}$ (M^{-1} ms^{-1})	-	1×10^5
	$k_{\mathrm{B,off}}$ (ms^{-1})	-	0.02
	B_{T} (µM)	0	10,000
	$Ca_{\mathrm{T}\infty}$ (µM)	5	5
result of Eq. 3A-4	B_{global} (µM)	0	9,995
	Ca_{global} (µM)	5	~0
diffusion	D_{Ca} (µm^2 ms^{-1})	0.4	
	D_{B} (µm^2 ms^{-1})	0.2	
channel gating	i_{Ca} (pA)	0.75	
	t_{open} (ms)	4	
	t_{closed} (ms)	6	

Table S1: Reaction-diffusion parameters for nanodomain Ca^{2+} modeling.   The buffer association and diffusion parameters are from (Kits et al., 1999), and the channel gating parameters are based upon our single-channel data for $Ca_V 1.3$.

The reaction diffusion system specified by Equations 3A-2, 3A-3 and 3A-4 comprise a set of partial differential equations for which a general analytic solution in time and space—which would fully specify the spatiotemporal details of $[Ca^{2+}]$—is not known. Three different approaches to analyze this system are nonetheless possible:

1. If we only consider the steady-state $[Ca^{2+}]$ profile, an analytic solution can be obtained (Stern, 1992):

$$Ca_{\text{spike}}\left(r_{\text{d}}\right) = \lim_{t \to \infty}\left[Ca^{2+}\right] = \frac{i_{\text{Ca}}}{4 \cdot \pi \cdot F \cdot D_{\text{Ca}} \cdot r_{\text{d}}} \cdot exp\left(\frac{-r_{\text{d}}}{\sqrt{D_{\text{Ca}}/\left(k_{\text{B,on}} \cdot B_{\text{T}}\right)}}\right) + Ca_{\text{global}} \qquad (3\text{A-}5)$$

This solution describes the decline of free Ca^{2+} concentration with increasing distance from the channel, $Ca_{\text{spike}}(r_{\text{d}})$, long after the onset of an ongoing channel opening. Note that here we define Ca_{spike} as a function of r_{d}, whereas the main text focuses on the value of Ca_{spike} at the position of CaM, $r_{\text{CaM}} \approx 10$ nm. Because CaM is constitutively attached to the channel, r_{CaM} does not change, and the main text treats Ca_{spike} as a constant, whose value is $Ca_{\text{spike}}(r_{\text{CaM}})$. Though useful, this steady-state solution has two major limitations. First, it does not give the temporal details of Ca^{2+} transients induced by channel gating, and these details are necessary features for understanding Ca^{2+} decoding. Second, this solution is only accurate if buffer consumption is negligible ('excess-buffer approximation'). Though this approximation will turn out to be valid, it must be verified by other means. Thus, this approach by itself is insufficient.

2. A finite-element method (FEM) (Figure S7A) considers the cytoplasmic space as a series of thin hemispherical shells; a configuration that enables numerical determination of the free Ca^{2+} concentration as a function of space *and time*. Hence, this output furnishes a more complete view of nanodomain Ca^{2+} than the analytic solution above. A further advantage is that the finite-element approach does not require the excess buffer approximation, so the FEM can be used to verify the validity of this approximation. Still, this method only describes average Ca^{2+} concentrations (averaged over many nanodomains), and does not comment on the stochasticity of nanodomain Ca^{2+}.

3. To characterize the stochastic nature of Ca^{2+}, we can turn to a Stochastic Monte-Carlo Method (SMCM), which tracks the motion and interaction of individual ions (Figure S7B). This method is the most realistic, and explicitly reveals the consequences of the sparse integer-valued nature of Ca^{2+} ions within the nanodomain. The SMCM approach may, however, entail substantial computational costs.
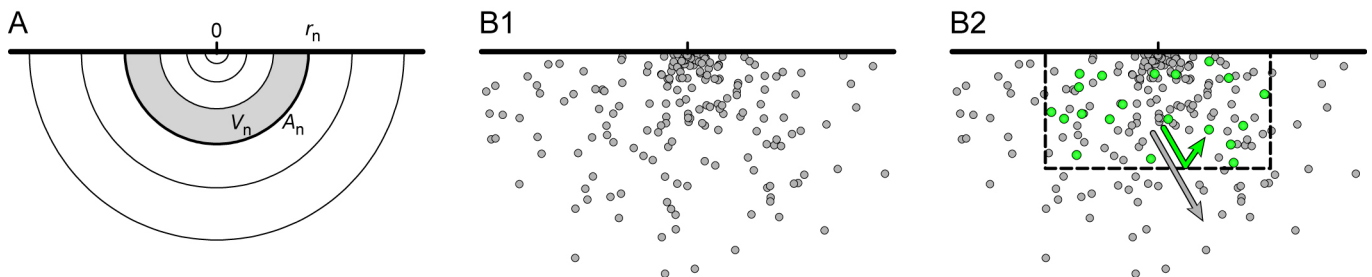
Figure S7 Numerical methods for modeling nanodomain Ca^{2+} signals. (A) Finite Element Method (FEM) discretizes space into N well-mixed 'shells.' Shell n (with gray shading) has volume V_{n}, outer surface area A_{n}, and is bounded by r_{n} and $r_{\text{n-1}}$. (B) Stochastic Monte Carlo Method (SMCM) tracks the diffusive movement of individual ions. Local Ca^{2+} ions (gray circles) originate from the channel, and freely diffuse in all directions except for a reflective surface at the membrane. Global Ca^{2+} ions (B2, green circles) are always present, and are bounded by a box (dashed line in B2) which is exclusively reflective to global ions.

In Sections 3B-C, we will calculate the spatiotemporal nanodomain Ca^{2+} signals in question using all three methods, and demonstrate that all three yield consistent results. This will set the stage for in-depth testing of slow CaM and SQS mechanisms under both continuum and stochastic regimes.

3B. Nanodomain Ca^{2+} signals by the Finite-Element Method

Here, we use the finite-element method (FEM) to calculate the spatiotemporal features of Ca^{2+} signals near a channel which is gating open and closed. The basic strategy is to convert the system of two partial differential equations (Equation 3A-2), which describes the two spatiotemporally varying state variables, $[Ca^{2+}](r_d, t)$ and $[B](r_d, t)$, into a simpler system of ordinary differential equations for state variables that only vary with time. This is accomplished by discretizing space into a finite number of well-mixed, hemispheric compartments ('shells'), which are arranged to exploit the spatial symmetry of this problem (Figure S7A). Each compartment ($n = 1, 2, \ldots, N$) contains time-varying free-calcium and free-buffer concentration, $[Ca^{2+}]_n(t)$ and $[B]_n(t)$. Because each compartment is well-mixed, the diffusion terms of Equation 3A-2 can be replaced with finite-difference approximations, thus eliminating spatial derivatives. This system now takes the form of $2N$ ordinary differential equations (Kits et al., 1999):

$$\frac{d[Ca^{2+}]_n}{dt} = \frac{D_{Ca}}{V_n}\left[\frac{A_{n-1}}{(r_n - r_{n-2})/2}\left([Ca^{2+}]_{n-1} - [Ca^{2+}]_n\right) - \frac{A_n}{(r_{n+1} - r_{n-1})/2}\left([Ca^{2+}]_n - [Ca^{2+}]_{n+1}\right)\right]$$
$$- k_{B,on} \cdot [Ca^{2+}]_n \cdot [B]_n + k_{B,off} \cdot (B_T - [B]_n) + J_n$$

$$\frac{d[B]_n}{dt} = \frac{D_B}{V_n}\left[\frac{A_{n-1}}{(r_n - r_{n-2})/2}\left([B]_{n-1} - [B]_n\right) - \frac{A_n}{(r_{n+1} - r_{n-1})/2}\left([B]_n - [B]_{n+1}\right)\right] \qquad \text{(3B-1)}$$
$$- k_{B,on} \cdot [Ca^{2+}]_n \cdot [B]_n + k_{B,off} \cdot (B_T - [B]_n)$$

where the state-variables $[Ca^{2+}]_n(t)$ and $[B]_n(t)$ are defined for $n = 1, 2, \ldots, N$; the shell radii r_n are defined as $0 = r_0 < r_1 < r_2 < \ldots < r_N < r_{N+1}$; and the shell surface area and volume are defined as: $A_n = 2\pi r_n^2$ and $V_n = 2\pi / 3 (r_n - r_{n-1})^3$.

To account for the first set of boundary conditions at the channel (Equation 3A-3), we define $r_0 = 0$ to make $A_0 = 0$. In this way, there is zero diffusive flux at $r_d = 0$. The remaining aspect of this set of boundary conditions pertains to the Ca^{2+} influx through the channel, and this constraint is satisfied by setting

$$J_n = \begin{cases} \dfrac{i_{Ca}}{2 \cdot F \cdot V_1} & \text{if } n = 1, \text{ and channel is open} \\ 0 & \text{otherwise} \end{cases} \qquad \text{(3B-2)}$$

The second set of boundary conditions (Equation 3A-4), relating to constraints far from the channel, is implemented by defining an additional shell $N + 1$ with the special properties

$$[Ca^{2+}]_{N+1} = Ca_{global} \qquad\qquad [B]_{N+1} = B_{global} \qquad\qquad \text{(3B-3)}$$

Thus, the free calcium and buffer concentrations within this shell are clamped to the global concentrations defined in Equation 3A-4. If r_N is large enough, Equation 3B-3 accurately approximates Equation 3A-4.

The choice of r_n and N are optimized to maximize accuracy and computational speed. The well-mixed shell approximation is only valid if the concentration gradient across two neighboring shells is small. One way to accomplish this is to make all shells very thin, while keeping shell $N+1$ (the global boundary condition shell, Equation 3B-3) far from the channel. This approach would require a very large N, whereas considerations of computational speed would favor a relatively small N. We therefore adopt a second approach, which optimizes these competing factors. Here, the shells are densely spaced near the channel (improving accuracy where the concentration gradients are steepest), but progressively less tightly spaced with increasing distance from the channel (enabling a large final shell radius without incurring prohibitive computational costs). In particular, the shell spacing is given by $r_n = n^2 \cdot 0.05$ nm, with $N = 200$, enabling run times of a few minutes.
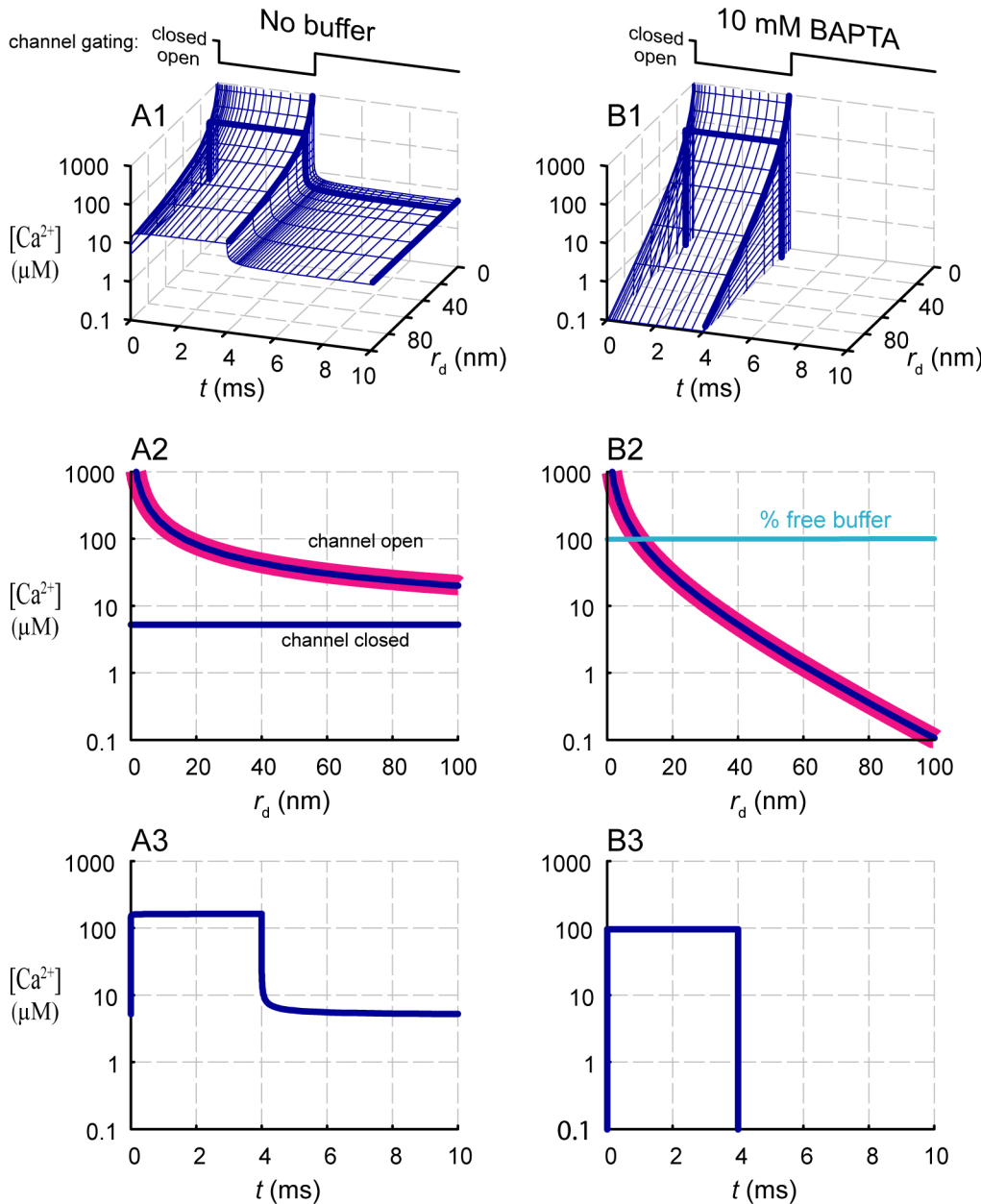
Figure S8 Results of the FEM with parameters in Table S1. The Ca^{2+} channel is repeatedly gated open for 4 ms and closed for 6 ms, altogether for six cycles. Results for the final open-closed cycle of the channel are shown for the no-buffer condition (A) as well as the 10 mM BAPTA case (B).

(A1, B1) $[Ca^{2+}]$ as a function of space (r_d) and time (t). Key aspects are emphasized with heavy blue lines, which are re-plotted below for clarity.

(A2, B2) Steady-state profile of $[Ca^{2+}]$ as a function of r_d, corresponding to the end of the open and closed periods. FEM results (blue curves) are overlaid with the analytic result $Ca_{spike}(r_d)$ from Equation 3A-5 (thick magenta curves). For (B2), the fraction of unbound BAPTA is shown in cyan.

(A3, B3) Temporal profile of $[Ca^{2+}]$ at $r_d = 10$ nm, the approximate location of CaM.

Figure S8 shows the results of FEM numerical simulations, using initial conditions $[Ca^{2+}]_n = Ca_{global}$, and $[B]_n = B_{global}$, and the parameters in Table S1. The Ca^{2+} channel is repeatedly gated open for 4 ms and

closed for 6 ms, altogether for six cycles. Under this configuration, the FEM equations (3B-1, 3B-2, and 3B-3) are numerically integrated for 60 ms using the MATLAB ode23tb solver. Results for the final 10 milliseconds of these simulations are shown. Panel A displays results obtained in the absence of buffer, and panel B shows results in the presence of 10 mM BAPTA. The surface plots in panels A1 and B1 summarize the output of the FEM, where free Ca^{2+} concentration is plotted as a function of space (r_d) and time (t). Key aspects are emphasized with heavy blue lines, which are re-plotted in the panels below for clarity. Three significant results arise:

The first result concerns the lack of appreciable buffer consumption. In panels A2 and B2, we show the spatial $[Ca^{2+}]$ profiles (as a function of r_d) at the end of the open and closed periods, corresponding to steady-state conditions. In the absence of buffer (A2), the concentration profile at the end of the open period (blue curve, channel open) matches exactly with the analytic steady-state profile (thick magenta curve), as given by $Ca_{\mathrm{spike}}(r_d)$ from Equation 3A-5. Importantly, Equation 3A-5 also accurately predicts $Ca_{\mathrm{spike}}(r_d)$ under 10 mM BAPTA (B2), indicating that the excess buffer approximation, upon which Equation 3A-5 relies, is valid. In fact, direct FEM results indicate that the fraction of free BAPTA remains at essentially 100% over all r_d (B2, cyan curve). Thus, BAPTA is replenished by diffusion much more rapidly than it is consumed by Ca^{2+} binding.

The second significant outcome concerns the temporal response of Ca^{2+}. The bottom panels (A3, B3) show the temporal profile of $[Ca^{2+}]$ at $r_d = 10$ nm, the approximate location of CaM. It is clear that $[Ca^{2+}]$ develops and decays on the microsecond timescale, resulting in nearly step-like Ca^{2+} signals, thus validating the simplified square-pulse Ca^{2+} signals used in main text Figures 1 and 2. To summarize, then, these FEM results confirm that the nanodomain Ca^{2+} signal can be well approximated as:

$$\left[Ca^{2+}\right](r,t) \approx \begin{cases} Ca_{\mathrm{global}} & \text{(Equation 3A-5)} & \text{if channel is closed} \\ Ca_{\mathrm{spike}}(r) & \text{(Equation 3A-6)} & \text{if channel is open} \end{cases} \qquad \text{(3B-4)}$$

The last significant result relates to the insensitivity of Ca_{spike} to buffering. Specifically, the value of Ca_{spike} at the location of CaM, $Ca_{\mathrm{spike}}(r_d = 10$ nm) is always on the order of ~100 μM, regardless of buffering even with 10 mM BAPTA. This result also holds if endogenous buffers, which are moderate in comparison to 10 mM BAPTA, are taken into account (verified numerically, data not shown), and confirms prior analyses of this configuration (Neher, 1998; Sherman et al., 1990). Because of the insensitivity of Ca_{spike} to endogenous buffering, and because endogenous buffers had no significant effect on the temporal aspects of nanodomain Ca^{2+}, we opted to focus upon the zero-buffer and 10 mM BAPTA conditions for computational efficiency, in particular for the stochastic simulations in the next section.

3C. Nanodomain Ca^{2+} signals by the Stochastic Monte-Carlo Method

A Stochastic Monte-Carlo Method (SMCM) is fundamentally different than analytic or finite-element (FEM) approaches, in that the movement of individual ions is explicitly modeled. This core difference distinguishes the SMCM in two important ways. First, the SMCM explicitly treats ions as discrete non-divisible entities, whereas the FEM is founded upon average concentrations, which may correspond to a fraction of an ion if small volumes are considered. Second, a SMCM can give different outcomes on each trial, whereas the FEM always yields the identical mean result. These two distinctives can be illustrated with a simple example. If we consider the roll of a die, each SMCM simulation would result in any integer between 1 and 6, whereas the FEM would always return the mean-value of 3.5, a number which could never actually occur on any single roll.

To address the stochastic nature of nanodomain Ca^{2+} signals and their decoding, we have undertaken a SMCM approach founded on the algorithms used by MCell (Stiles and Bartol, 2001; Stiles et al., 1996). This section will focus on nanodomain Ca^{2+} signals generated by the SMCM, and the next sections (3D-E) will extend the approach to the effects of stochasticity on local/global Ca^{2+} decoding mechanisms.

The SMCM is implemented in discrete-time, with time step $= \Delta t$. The movement of each ion during Δt is calculated using random numbers drawn from a probability distribution adhering to Fick's law, which states:

$$\frac{\partial\left[Ca^{2+}\right]}{\partial t} = D_{Ca} \cdot \nabla^2\left[Ca^{2+}\right] \tag{3C-1}$$

This can be achieved as follows. Over a time interval, Δt, the displacement of a Ca^{2+} ion is given by the displacement vector $\Delta \boldsymbol{v}$, whose Cartesian coordinates are $(\Delta x, \Delta y, \Delta z)$. The z-axis intersects the channel and is perpendicular to the membrane, with $z = 0$ corresponding to the plane of the membrane. Increasingly positive z values refer to cytoplasmic locations that are progressively distant from the channel. Because diffusion is isotropic, it is advantageous to consider $\Delta \boldsymbol{v}$ in spherical coordinates, as given by radial distance r_Δ ($= \sqrt{\Delta x^2 + \Delta y^2 + \Delta z^2}$), and direction specified by angles ϕ ($= \tan^{-1}\left(\sqrt{\Delta x^2 + \Delta y^2}\big/\Delta z\right)$) and θ ($= \tan^{-1}(\Delta y/\Delta x)$), drawn from the following probability density functions (Stiles and Bartol, 2001). First, the distance, r_Δ, is determined by:

$$r_\Delta = s \cdot \sqrt{4 \cdot D_{Ca} \cdot \Delta t} \qquad p(s) = \frac{4}{\sqrt{\pi}} \cdot s^2 \cdot exp\left(-s^2\right) \tag{3C-2A}$$

where the random variable s is a unitless standardized distance, and $p(s) \cdot ds$ is the probability that s adopts a value between s and $s + ds$. The actual radial displacement r_Δ (in units of μm) can be obtained by multiplying s with the 'length constant' $\sqrt{4 \cdot D_{Ca} \cdot \Delta t}$ (in units of μm).

Second, because isotropic diffusion is equal in all directions, θ and ϕ are determined by:

$$p(\theta) = \begin{cases} \dfrac{1}{2\pi} & 0 < \theta < 2\pi \\ 0 & \text{otherwise} \end{cases} \qquad p(\phi) = \begin{cases} \dfrac{\sin(\phi)}{2} & 0 < \phi < \pi \\ 0 & \text{otherwise} \end{cases} \tag{3C-2B}$$

θ and ϕ uniformly sample from the surface of a unit sphere.

Given these rules, the displacement of an ion over one time interval (Δt) is given by selecting random values for r_Δ, θ, and ϕ (according to Equation 3C-2), and converting to Cartesian coordinates: $\Delta \boldsymbol{v} = (\Delta x, \Delta y, \Delta z) = r_\Delta (\sin\phi\cos\theta, \sin\phi\sin\theta, \cos\phi)$. Figure S9 gives an intuitive sense of these movements. A molecule's displacement over Δt follows a spherically symmetric Gaussian distribution. Figure S9 only shows a slice through this three-dimensional distribution in the plane parallel to the membrane (i.e. the $\Delta z = 0$ plane).

To speed computation, a large number of random standardized distances (s) and random unit direction vectors, $\boldsymbol{u} = (\sin\phi\cos\theta, \sin\phi\sin\theta, \cos\phi)$, are pre-calculated and stored
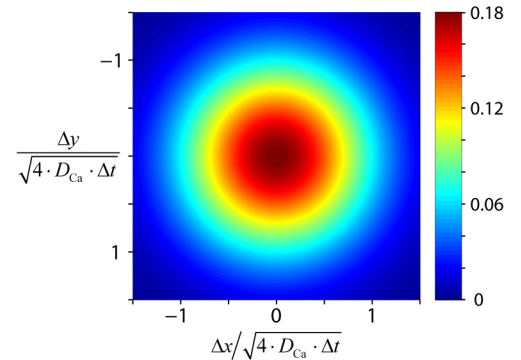
Figure S9. Diffusion over the time interval Δt is implemented by displacing each ion according to the probability distribution shown. Note that Δx and Δy are normalized by the length constant $\sqrt{4 \cdot D_{Ca} \cdot \Delta t}$, and that only a slice through the $\Delta z = 0$ plane is shown.

20

in two lookup tables. To ensure that the unit vectors contain no directional bias, the second lookup table is reflected 8-fold along the three Cartesian axes (Stiles and Bartol, 2001). At each time step, for each Ca^{2+} ion, $\boldsymbol{u}$ and s are chosen randomly from these lookup tables, and the ion position is displaced by $\Delta\boldsymbol{v} = \boldsymbol{u} \cdot s \cdot \sqrt{4 \cdot D_{Ca} \cdot \Delta t}$. Diffusion for BAPTA would utilize the same lookup tables as Ca^{2+}, but would use the shorter length-constant $\sqrt{4 \cdot D_B \cdot \Delta t}$.

Collisions with the plasma membrane result in reflections at the $z = 0$ plane. As for Ca^{2+} sources, the channel is cast as a point generator of Ca^{2+} ions located at the origin (Figure S7B1). The probability of generating a new ion at each time step is:

$$p_{new\_ion} = \begin{cases} \dfrac{i_{Ca}}{2 \cdot F} \cdot N_A \cdot \Delta t & \text{if channel is open} \\ \\ 0 & \text{otherwise} \end{cases}$$

(3C-3)

where F is Faraday's constant and N_A is Avogadro's number. Because a newly generated Ca^{2+} ion can be released at any time during the Δt interval, it is displaced according to a modified version of Equation 3C-2, where the effective time step (Δt^*) is a random number, uniformly distributed over the interval $[0, \Delta t]$. Thus, for the first diffusion step, a random-valued length constant of $\sqrt{4 \cdot D_{Ca} \cdot \Delta t^*}$ is used. However, for all future time steps, the length-constant is fixed at $\sqrt{4 \cdot D_{Ca} \cdot \Delta t}$.

To model the global Ca^{2+} signal, we distinguish Ca^{2+} ions which originate from the channel ('local Ca^{2+} ions') from those which originate elsewhere ('global Ca^{2+} ions'). Local Ca^{2+} ions diffuse freely, except for a reflective surface at $z = 0$. Global Ca^{2+} ions are present from the beginning of the simulation, and are constrained to remain within a bounding box, which is invisible to local Ca^{2+} ions but reflective to global Ca^{2+} ions (Figure S7B2). Aside from these two differences, all other aspects of local and global Ca^{2+} ions are identical (i.e. diffusion, buffering, binding to CaM). A large number of global ions is used (100), and the volume of the box is adjusted to set the global ion concentration to 5 μM.

The time required for computations becomes excessive if the simulation duration and/or the number of diffusing ions is large. For a one-second simulation (necessary for testing the decoding mechanisms), with $i_{Ca} = 0.75$ pA, and $P_O = 0.4$ (Table S1), $\sim10^6$ Ca^{2+} ions would be generated. To accurately model binding between Ca^{2+} and the CaM/channel complex (explained in the next section), the largest acceptable time step is $\Delta t = 1 \times 10^{-7}$ sec. This corresponds to $\sim5 \times 10^{12}$ diffusion movements per simulation, which would take ~2-5 months even on an optimized platform such as MCell2 (Stiles and Bartol, 2001; Stiles et al., 1996). To speed computation, ions could be discarded after reaching a certain distance from the channel; essentially creating a Ca^{2+} sink at some distance. However, since this could degrade the validity of the results, we instead utilize a 'time-skipping' algorithm, which exploits the fact that Equation 3C-2 can accurately predict diffusive movements for large time steps, without the need to iterate many smaller steps. This idea is implemented in MCell3 (Kerr et al., submitted), and is here customized for the channel nanodomain problem. The smallest time step $(\Delta t = 1 \times 10^{-7}$ sec) is only used for Ca^{2+} ions within an 'action radius' of the channel, where only these ions can potentially bind the CaM/channel complex within a single Δt. Ions outside the action radius are moved less frequently, with $\Delta t_k = 2^k \cdot \Delta t$, where k indicates a group index. Ions are categorized into group $k > 0$ only if their distance from CaM is large enough to preclude interaction with CaM within Δt_k. Though dynamic reassignment of ions into groups adds some computational overhead, it is far remunerated by the $\sim10,000$-fold reduction in total number of diffusion movements required per simulation. Implementation of this algorithm in MATLAB enabled completion of a 1-sec simulation involving 10^6 ions in 1-2 hours, thus motivating development of customized software for this particular application.

As for Ca^{2+} buffering, we consider either zero-buffer or 10 mM BAPTA scenarios, so as to mirror the FEM simulations in Figure S8. For the latter case, modeling of individual BAPTA molecules would pose a severe computational challenge, given the high concentration of BAPTA and infinite-half-space geometry. Furthermore, modeling of individual buffer molecules would preclude use of the time-skipping algorithm, since every Ca^{2+} ion could potentially bind to nearby buffer molecules, requiring all molecules to use the finest time step of 1×10^{-7} sec. To circumvent these challenges, we utilize the validity of the excess-buffer approximation under these conditions (Figure S8B2). This approximation allows a simple implementation of Ca^{2+} buffering, by switching Ca^{2+} ions between 'free' and 'buffer-bound' conformations, according to

$$Ca \underset{k_{B,off}}{\overset{k_{B,on} \cdot B_T}{\rightleftharpoons}} CaB \tag{3C-4}$$

This scheme exploits the fact that the free BAPTA concentration is everywhere $\sim B_T$, yielding a *fixed* effective buffer association rate constant of $k_{B,on} \cdot B_T$. The probability of Ca^{2+} switching between free and buffer-bound conformations after a time $\Delta t_k = 2^k \cdot \Delta t$ is computed via the following matrix exponentials

$$prob(Ca \to CaB) = \cdot \begin{bmatrix} 0 & 1 \end{bmatrix} \cdot expm\left(\begin{bmatrix} -k_{B,on} \cdot B_T & k_{B,off} \\ k_{B,on} \cdot B_T & -k_{B,off} \end{bmatrix} \cdot 2^k \cdot \Delta t \right) \cdot \begin{bmatrix} 1 \\ 0 \end{bmatrix}$$

$$\tag{3C-5}$$

$$prob(CaB \to Ca) = \cdot \begin{bmatrix} 1 & 0 \end{bmatrix} \cdot expm\left(\begin{bmatrix} -k_{B,on} \cdot B_T & k_{B,off} \\ k_{B,on} \cdot B_T & -k_{B,off} \end{bmatrix} \cdot 2^k \cdot \Delta t \right) \cdot \begin{bmatrix} 0 \\ 1 \end{bmatrix}$$

Matrix exponentials are pre-calculated for all values of $k = 0 \ldots 100$. This pre-calculation enables rapid implementation of this buffering algorithm, which is compatible with our time-skipping methodology. Buffered Ca^{2+} ions diffuse with the slower diffusion coefficient, D_B (Table S1).

Given this setup, we perform SMCM simulations that parallel the FEM computational experiments above. The system is driven by repetitive 10-msec cycles in which the channel gates open for 4 msec, and closed for 6 msec. In each simulation, one-hundred of these 10-msec cycles are delivered in succession, yielding a total simulation length of one second. The simulations are run with local and global Ca^{2+} signals present, both for the no buffer and 10 mM BAPTA case. Ten simulations are performed for each buffering condition. To ensure accurate diffusion down to the $\Delta t = 1\times10^{-7}$ sec time resolution for all ions within 100 nm of the channel, the action radius was set >100 nm.

To validate our SMCM algorithms, we calculate the average Ca^{2+} concentrations produced, so as to permit direct comparison with FEM results. These averages are calculated by defining thin hemispheric sampling shells (2 nm in thickness) centered at distances from the pore of 5, 10, 20, 30, 50, 70 and 100 nm. The free Ca^{2+} concentration within each of the sampling shells is then given by:

$$\left[Ca^{2+} \right](r_{shell}, t) = \frac{(\text{# of ions in shell at time } t)}{N_A \cdot (\text{volume of shell})} = \frac{(\text{# ions with } |r_{ion} - r_{shell}| < 1\text{nm, at time } t)}{N_A \cdot \frac{2}{3}\pi \cdot \left[(r_{shell} + 1\text{nm})^3 - (r_{shell} - 1\text{nm})^3 \right]} \tag{3C-6}$$

Using this approach, mean Ca^{2+} concentrations, averaged over 1,000 channel gating cycles, are derived.

Figure S10 compares the SMCM results to the FEM results described above (Figure S8). The format is identical to that in Figure S8, such that Figure S10A pertains to the no buffer condition, and Figure S10B to the 10 mM BAPTA case. The FEM outputs are reproduced in blue, and the SMCM data are shown in red. Results from the two methods are essentially identical. In particular, the SMCM waveforms nicely overlay the overall spatiotemporal surface of the FEM (A1, B1); the spatial profiles at steady state (A2, B2) are the same; and comparisons of temporal waveforms at 10 nm from the pore (A3, B3) are identical. The precise agreement of outputs from SMCM and FEM computations validates our implementation of both methods.
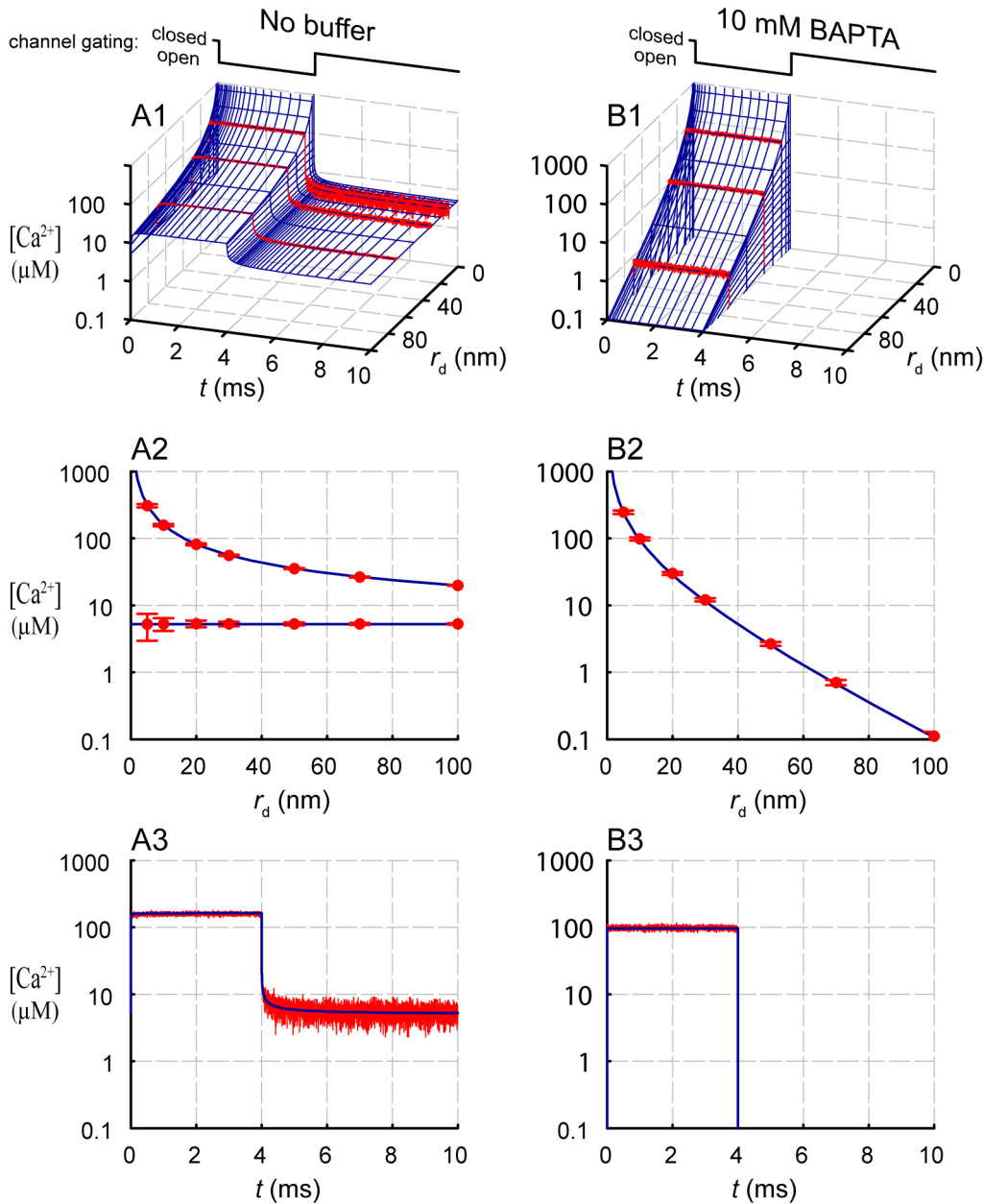

Figure S10 Results of the SMCM. The Ca^{2+} channel is repeatedly gated open for 4 ms and closed for 6 ms, altogether for 1000 cycles. The spatiotemporal free Ca^{2+} concentrations, averaged over the 1000 cycles, are shown for the no-buffer condition (A) as well as the 10 mM BAPTA case (B).

(A1, B1) $[Ca^{2+}]$ as a function of space (r_d) and time (t). FEM results in blue, SMCM results in red.

(A2, B2) Steady-state profile of $[Ca^{2+}]$ as a function of r_d, corresponding to the end of the open and closed periods. FEM results in blue. SMCM results (red with error bars) show the mean ± standard deviation of data from the last millisecond of the open and closed periods.

(A3, B3) Temporal profile of $[Ca^{2+}]$ at $r_d = 10$ nm, the approximate location of CaM. FEM results in blue. SMCM results in red.

In the next section, we explicitly harness the stochastic output of the SMCM to test the slow CaM and SQS Ca^{2+} decoding mechanisms. Of note, 10 mM BAPTA simulations in which global Ca^{2+} ions (green circles in Figure S7B2) were omitted yielded identical results to those in Figure S10B (data not shown). This exemplifies the ability of 10 mM BAPTA to completely buffer out the global Ca^{2+} signal, and was exploited to further optimize the upcoming stochastic simulations under 10 mM BAPTA.

3D. Decoding Mechanisms: comparison of Monte-Carlo with continuum methods

Though the average Ca^{2+} signals produced by the SMCM are identical to those produced by the FEM, the stochastic fluctuations of these signals could potentially affect the behavior of local/global decoding mechanisms. This is tested directly with SMCM simulations of the slow-CaM and SQS mechanisms.
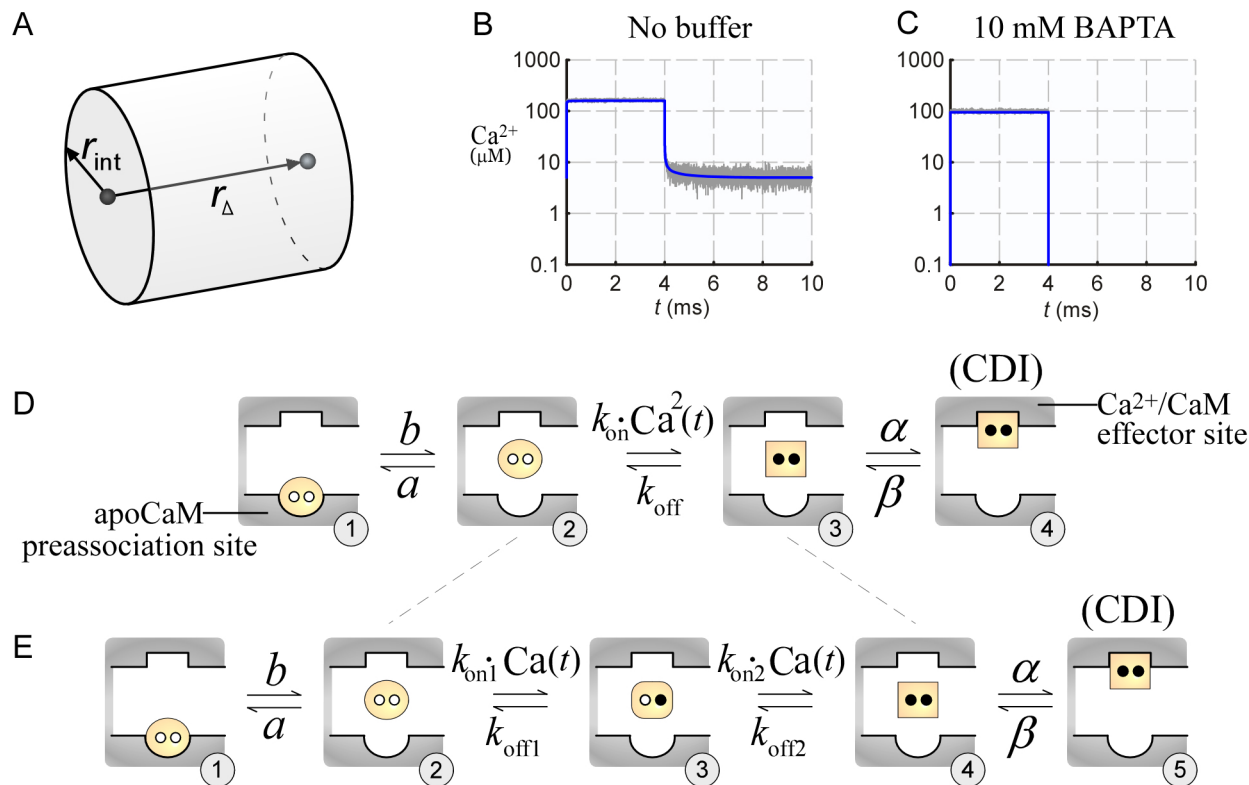
Figure S11 Stochastic reaction methodology. (A) Ca^{2+} ions trace out a cylindrical interaction volume during each diffusion step. A collision is said to occur if CaM lies within this cylinder. (B-C) Average Ca^{2+} concentration in the vicinity of CaM as calculated from collisions according to Equation 3D-1, averaged over 1000 channel gating cycles (gray). For reference, the FEM results are overlaid in blue. (D) Basic 4-state configuration, featuring simultaneous binding of two Ca^{2+} ions, reproduced from main paper Figure 2A. (E) Equivalent 5-state configuration, with sequential binding of Ca^{2+} ions.

Beyond the diffusion algorithms discussed in the previous section, investigating Ca^{2+} decoding mechanisms requires modeling stochastic interactions between Ca^{2+} and the CaM/channel complex. We therefore adopt MCell algorithms for biological reactions in solution (Kerr et al., submitted) into our custom MATLAB software. For each Ca^{2+} ion with movement as given by the displacement vector Δv in Equation 3C-2, a cylindrical interaction volume of radius r_{int} (a new parameter) and length r_Δ (Equation 3C-2) is traced out (Figure S11A). If this cylinder intersects CaM, we say that a collision occurred between the Ca^{2+} ion and CaM. Since CaM is constitutively affiliated with the channel, CaM is held at a fixed position, $r_{CaM} = 10$ nm from the channel pore ($(x, y, z) = (0, 0, 10$ nm$)$). We ensure that ions capable of colliding with CaM are updated at the finest time step ($\Delta t = 1 \times 10^{-7}$ sec) by setting the action radius greater than r_{CaM}.

To verify our implementation of this collision algorithm in MATLAB, we use a known equation relating the local free Ca^{2+} concentration to the average number of collisions (Kerr et al., submitted):

$$\left[Ca^{2+} \right](r_{CaM}, t) = \frac{\left(\text{average \# of collisions with CaM} \right)}{4 \cdot r_{int}^2 \cdot \sqrt{\pi \cdot D_{Ca} \cdot \Delta t} \cdot N_A} \tag{3D-1}$$

In a validation test, Ca^{2+} collisions with CaM are counted, without allowing CaM to bind Ca^{2+}. The result of Equation 3D-1, averaged over 1,000 open/closed gating cycles, is plotted in the absence of buffer (Figure S11B, gray) and in the presence of 10 mM BAPTA (Figure S11C, gray). The gray traces precisely overlay the mean Ca^{2+} concentration waveforms of FEM computations at r_{CaM}, thus verifying our implementation of the collision algorithm.

To allow compatibility of our decoding mechanisms with the SMCM, we create equivalent 5-state models, wherein the simultaneous binding of two Ca^{2+} ions (Figure S11D) is split into two sequential, single-binding steps (Figure S11E). The sequential parameters are chosen to maintain the cooperative nature of Ca^{2+} binding, as well as the kinetics and affinity of each lobe of CaM (Table S2). The equivalent 5-state model is necessary for compatibility with the first-order stochastic reaction methodology (Figure S11A), in which interaction radii and time steps are chosen to minimize the probability of simultaneous collisions (Kerr et al., submitted). Given the equivalent 5-state mechanisms, the transition probability rules by which Ca^{2+} collisions drive conformational changes during a single time step (Δt) are the following.

$$prob(state\ i \to j) = \Delta t \cdot \begin{bmatrix} 1-b & a & 0 & 0 & 0 \\ b & 1-a-k_{on1} \cdot C & k_{off1} & 0 & 0 \\ 0 & k_{on1} \cdot C & 1-k_{off1}-k_{on2} \cdot C & k_{off2} & 0 \\ 0 & 0 & k_{on2} \cdot C & 1-k_{off2}-\alpha & \beta \\ 0 & 0 & 0 & \alpha & 1-\beta \end{bmatrix}_{column\ i,\ row\ j}$$

where
$$C = \begin{cases} \dfrac{1}{4 \cdot r_{int}^2 \cdot \sqrt{\pi \cdot D_{Ca} \cdot \Delta t \cdot N_A}} & \text{if a collision occurs during } \Delta t \\[2em] 0 & \text{otherwise} \end{cases}$$

(3D-2)

Note that the average value of C is equivalent to the local Ca^{2+} concentration in the vicinity of CaM, as can be appreciated by comparison with Equation 3D-1. Equation 3D-2 stipulates that transitions which involve CaM binding Ca^{2+} are only allowed when a collision occurs. Once a Ca^{2+} ion binds to CaM, it is not allowed to diffuse, but rather is frozen at the end of its diffusion trajectory. Subsequently, if a model transition occurs which corresponds to release of this bound Ca^{2+} ion, the ion is simply allowed to diffuse starting from its frozen location. Such an algorithm obviates the need for more sophisticated placement of released ions (Kerr et al., submitted), since it exactly produces the theoretical ideal of microscopic reversibility. Finally, it is necessary to ensure that every element of the transition matrix in Equation 3D-2 is less than one, since probabilities cannot exceed one. The elements that do not include C are guaranteed to satisfy this constraint, given the small Δt of 10^{-7} sec, and the modest magnitudes of Ca^{2+}-independent rate constants. For terms with C, we consider that k_{on2} is always larger than k_{on1} for both the C-lobe and N-lobe models. Hence, each element of the transition matrix will be less than unity if the term containing $k_{on2} \cdot C \cdot \Delta t$ is less than unity. This is equivalent to the condition

$$r_{int} > \sqrt{\frac{k_{on2} \sqrt{\Delta t}}{4 \cdot N_A \cdot \sqrt{\pi \cdot D_{Ca}}}}$$

(3D-3)

Given the dimensions of a nanodomain, r_{int} is chosen as small as possible while satisfying Equation 3D-3. This corresponds to r_{int} = 6 nm for the N-lobe, and r_{int} = 5 nm for the C-lobe.

To verify the results of main paper Figure 2, we ran the 5-state C- and N-lobe models under conditions of zero-buffer and 10 mM BAPTA, with several channel open probabilities. The diffusion/buffering conditions are summarized in Table S1, and the channel gating and decoding parameters and are in Table S2. Each condition was repeated 75-200 times, with different random number seeds.

		C-lobe	N-lobe
CaM/channel binding	a (ms^{-1})	60	0.4
	b (ms^{-1})	0.04	0.004
	α (ms^{-1})	0.5	0.1
	β (ms^{-1})	0.05	0.01
CaM/Ca^{2+} binding (simultaneous)	k_{on} (M^{-2} ms^{-1})	1.2×10^{10}	3.7×10^{12}
	k_{off} (ms^{-1})	0.003	3
CaM/Ca^{2+} binding (sequential)	k_{on1} (M^{-1} ms^{-1})	1.6×10^{6}	6×10^{6}
	k_{on2} (M^{-1} ms^{-1})	6×10^{6}	9×10^{6}
	k_{off1} (ms^{-1})	600	9
	k_{off2} (ms^{-1})	0.004	4.5
channel gating, and model conditions	$P_{O,}$ zero buffer	0.4	0.4
	$P_{O,}$ 10 BAPTA	0.4, 1	0.2, 0.4, 0.6, 0.8, 1
	t_{open} (ms)	$10 \cdot P_O$	
	t_{closed} (ms)	$10 \cdot (1-P_O)$	

Table S2: Parameters for SMCM simulations of slow CaM (C-lobe) and SQS (N-lobe) mechanisms. Rate constants defined in Figure S11D-E; those in Figure S11D are identical to main text Figure 2. CaM/channel binding rates satisfy slow-CaM and SQS regimes; CaM/Ca^{2+} binding rates are consistent with those of CaM in free solution (Bayley et al., 1984; James et al., 1995; Martin et al., 1985; Teleman et al., 1986); and channel gating parameters correspond to our single-channel data and the parameters T_U and T_B from our voltage-block protocol.

Figure S12 compares the extent of CDI produced by the C-lobe (slow-CaM) mechanism in response to stochastic Ca^{2+} inputs (its 'stochastic response') with its response to continuum Ca^{2+} inputs ('continuum response'). Figure S12A1 shows the no-buffer $P_O = 0.4$ case. The top row overlays the average stochastic Ca^{2+} signal (gray trace) with its step-function continuum approximation (black). The bottom row overlays the average stochastic response of the 5-state C-lobe model (red trace) with the continuum response of the same model (black curve), as well as the continuum response of the original 4-state C-lobe model (gray curve) used in main text Figures 2C-D. As can be seen, the results of all three methods agree well. All three methods also agree under conditions of 10 mM BAPTA, both at $P_O = 0.4$ and $P_O = 1$ (Figure S12A2-A3). Finally, Figure S12B demonstrates that the steady-state stochastic responses from these simulations (colored points with error bars) match well with main text Equation 1 (solid black curve). Note that the zero-buffer simulation is a lower-limit estimate of CDI at $P_O = 1$ (red arrow), as discussed in the main text. Overall, these results confirm that even when stochastic details are taken into account, the 'slow-CaM' mechanism is insensitive to buffering by 10 mM BAPTA, and its $CDI(\infty)$–P_O relation conforms to a saturating Michaelis-Menton profile.

For the N-lobe SQS decoding mechanism, we performed extensive stochastic simulations which fully agree with their continuum simulation counterparts. Figure S13 displays the results with format analogous to that in Figure S12. Under conditions of no buffering and $P_O = 0.4$, both the stochastic and continuum simulations exhibit strong CDI (Figure S13A1). Moreover, at the same $P_O = 0.4$, the addition of 10 mM BAPTA nearly eliminates CDI (Figure S13A2). Thus, the essential feature of the SQS mechanism is found to hold true, even when stochastic Ca^{2+} inputs are considered: intense yet intermittant ~100 μM local

signals produce little CDI, whereas weak enduring ~5 µM global signals produce strong CDI. To fully verify main text Equation 2, we ran numerous stochastic simulations at five different channel open probabilities under 10 mM BAPTA (Table S2). Strong CDI is evident at $P_O = 1$ (Figure S13A3, Figure S13B, blue), with significantly less CDI at $P_O \leq 0.8$ (Figure S13B). When viewed on a $CDI(\infty)$–P_O curve, the stochastic N-lobe simulations show unmistakable upward curvature (Figure S13B, data points with error bars), with remarkable correspondence to main text Equation 2 (solid black curve). Overall, Figures S12 and S13 establish that the N- and C-lobe mechanisms respond identically to stochastic and continuum Ca^{2+} inputs.
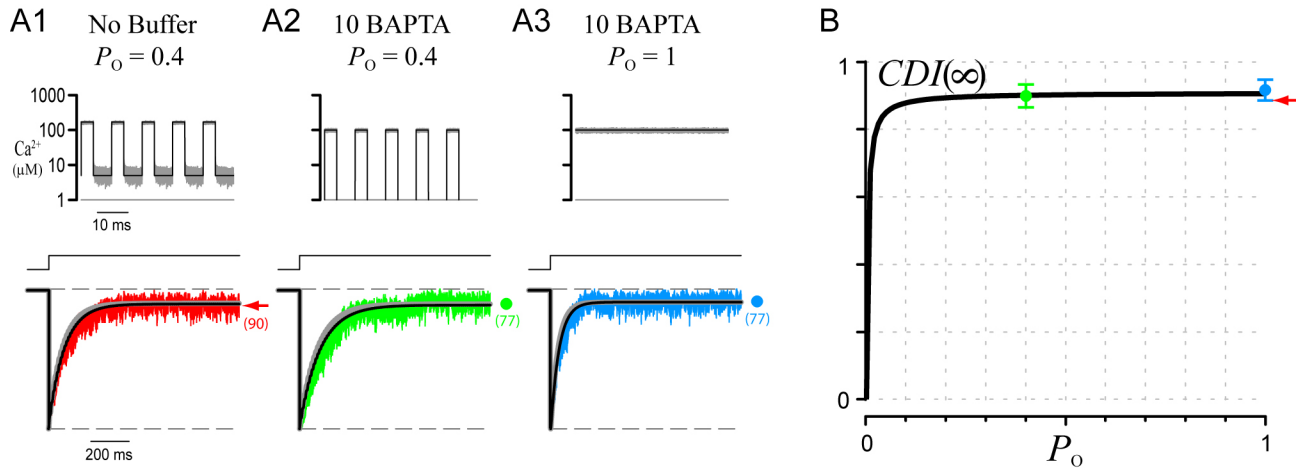

Figure S12 SMCM results for C-lobe slow-CaM decoding. (A, top) Stochastic Ca^{2+} input (gray) overlaid with continuum square-pulse approximation (black). Buffer and channel open probability are as stated at top. (A, bottom) For the SMCM, each condition was iterated many times (value of n is in parenthesis), and the fraction of runs which occupied state 5 (=CDI in Figure S11E) are shown as a function of time (colored traces, mean ± s.e.m.). This was directly compared to the continuum behavior of the same 5-state model (black trace) as well as the original 4-state model (gray trace) which is the model simulated in main paper Figure 2. See Supplementary Information 4F for details regarding continuum numerical simulations. (B) The steady-state extent of CDI reached by the SMCM (averaged over the final 100 ms) is plotted against channel P_O. 10 BAPTA simulations shown as colored symbols with error bars. Red arrow corresponds to the no-buffer simulation. Black curve is the $CDI(\infty)$–P_O relation predicted by main text Equation 1.
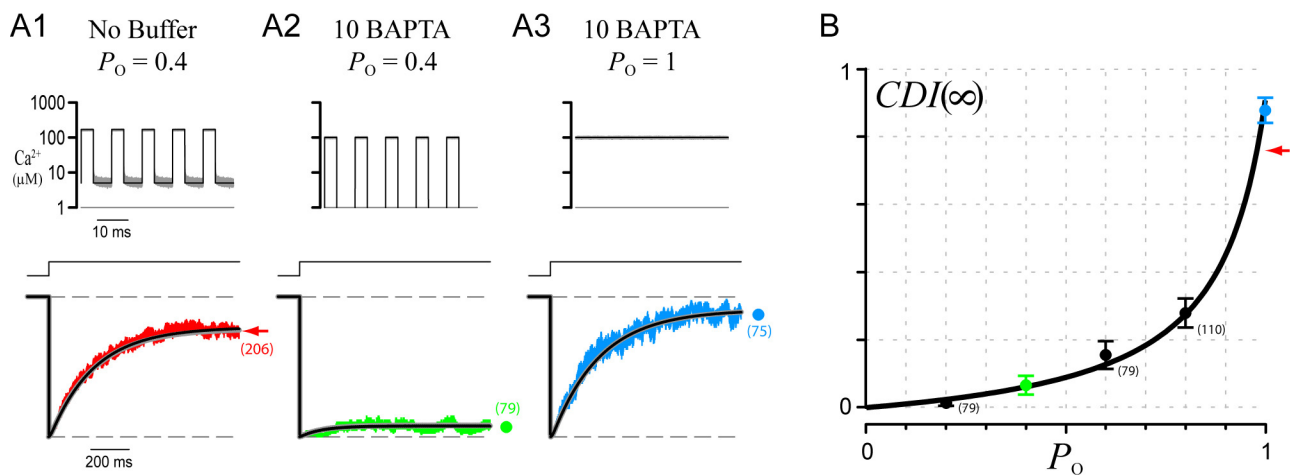
Figure S13 SMCM results for N-lobe SQS decoding, format as in Figure S12, with additional 10 BAPTA simulations (black symbols with error bars in panel (B)). Black curve in (B) is the $CDI(\infty)$–P_O relation predicted by main text Equation 2.

3E. Rationale for equivalence of stochastic and continuum simulations of decoding mechanisms
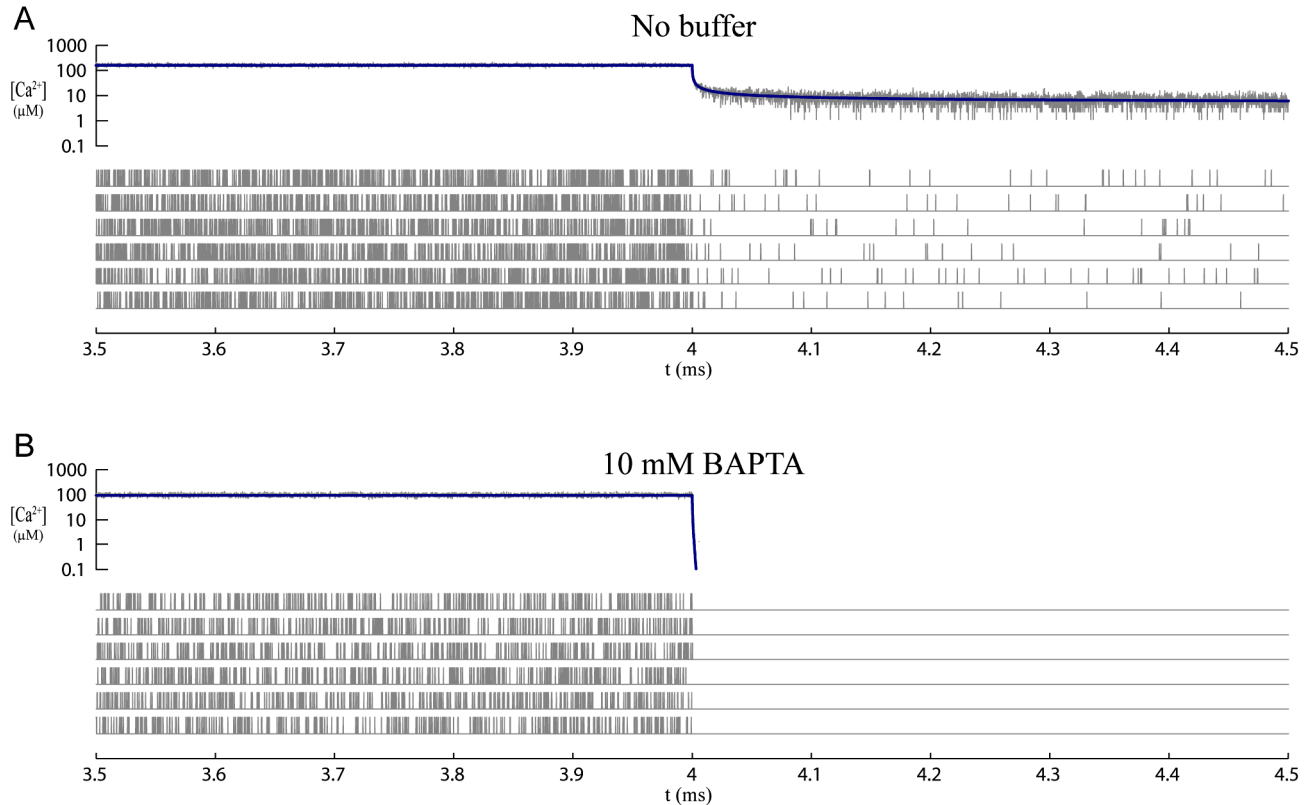
Figure S14 Stochasticity of collisions between Ca^{2+} and CaM viewed on an expanded time base. At the top of each panel is a reproduction of Figure S11B/C, showing the sub-microsecond decay of nanodomain $[Ca^{2+}]$ following a channel closure. Below are individual sweeps, which detail the time course of individual collisions between Ca^{2+} and CaM. These binary sweeps are sampled at $\Delta t = 1 \times 10^{-7}$ sec, and assume a value of one if at least one collision occurs during that time step. The incidence of multiple collisions is small ~5%, in accord with first-order binding methodology (Equation 3D-2).

Given the marked stochasticity of Ca^{2+} within the channel nanodomain, it might be unexpected that decoding mechanisms behave identically whether driven by stochastic or average Ca^{2+} inputs. This equivalence can be understood by examining the nature of stochastic Ca^{2+} fluctuations on an expanded timebase (Figure S14) under condtions of no buffering (A) and with 10 mM BAPTA (B). Fluctuations due to channel gating occur on the millisecond timescale, whereas fluctuations due to stochastic Ca^{2+} diffusion occur on the sub-microsecond timescale. This feature allows us to utilize the results of Section 2, where we prove that the C-lobe, which unbinds Ca^{2+} slowly relative to millisecond channel closings, essentially 'sees' only the average Ca^{2+} signal (averaged over channel gating). In the present case, the C-lobe would certainly be unable to track the much faster sub-microsecond stochastic fluctuations, and would again 'see' only this average Ca^{2+} signal. Since the average Ca^{2+} signal is identical for both the SMCM and FEM (Figure S10), it follows that the output of the slow-CaM mechanism would also be identical (Figure S12).

As for the N-lobe model, the SQS mechanism, which features rapid Ca^{2+} (un)binding, can exhibit remarkable sensitivity to the millisecond Ca^{2+} fluctuations induced by channel gating. The critical new insight is that though N-lobe Ca^{2+} (un)binding is rapid relative to the timescale of channel gating, it is nonetheless slow relative to the microsecond timescale of stochastic fluctuations. Thus, although the N-lobe can track channel-gating fluctuations, it essentially averages over stochastic fluctuations by analogy to the C-lobe analysis (Supplementary Information 2). Since the average Ca^{2+} signal is clearly the same

28

across records (Figure S14), it follows that the average stochastic N-lobe response will be identical to that produced by continuum methods.

In closing, Figure S14 gives a visual representation of the extraordinary selectivity supported by N-lobe decoding. Intense, densely-spaced Ca^{2+} collisions due to local Ca^{2+} signals (Figure S14B) fail to produce CDI, whereas sparse collisions from global Ca^{2+} signals, which persist during channel closings (Figure S14A, right), succeed to induce strong CDI.

4. Supplemental Experimental and Analysis Procedures

4A. Single channel ramp analysis

For each construct (main paper Figures 3C, 5B, 6A-B, and supplemental data Figures S19A, S19E), on-cell single-channel ramps were repeated with a repetition interval of 5-15 seconds. For any given patch, we recorded 50-200 sweeps. Patches containing single-channel activity were analyzed as follows:

(1) The leak for each sweep was approximated by a roughly linear smooth function (third-order polynomial with very low-magnitude nonlinear components) fit by eye to correspond to channel closings, and was subtracted from each trace.

(2) The unitary current relation, $i(V)$, was fit to the open-channel current level using the following GHK equation (Hille, 1984):

$$i(V) = -g \cdot (V - V_S) \cdot \frac{e^{\frac{-(V-V_s)}{zF/RT}}}{1 - e^{\frac{-(V-V_s)}{zF/RT}}} \tag{4A-1}$$

Unlike the leak fits, which were adjusted for each sweep, the same unitary current fit was used for all sweeps of a given patch. Furthermore, the key parameters, g and zF/RT, were held constant for all patches of a given construct, only allowing V_s, a surface-charge shift, to vary slightly from patch to patch.

(3) The leak-subtracted traces for each patch were averaged together, yielding an I-V curve. Blank sweeps were excluded from this average for two reasons: First, the presence of blank sweeps likely results from accumulation of voltage-dependent inactivation resulting from the fast repetition rate necessary to obtain sufficient data for single-channel analysis. This degree of cumulative VDI would not be present in voltage-block experiments which used 90 second repetition intervals. Second, blank sweeps represent single channels that are silent during the entire sweep. Channels in this state would not contribute to whole-cell current, and thus would not be represented in our measurement of CDI, which only detects the fraction of channels initially active that become inactivated during a sweep.

(4) The I-V curves obtained from different patches were averaged together. Since there was some variability in V_s across patches, we first calculated an average V_s for the construct, $V_{s,ave}$. Prior to averaging, the data from each patch was shifted slightly in voltage by the amount $V_{s,ave} - V_s$. An identical shift was applied for the unitary-current GHK relation of each patch, thus causing all patches to share a common GHK relation.

(5) The activation curve (P_O versus V) for each construct was determined by taking the ratio of the average I-V curve across all patches (from step 4) with the GHK relation.

The resulting activation curves provided an absolute measure of P_O, however, because of differences in surface charge shift between single-channel and whole-cell configurations, the curves needed to be calibrated in voltage. This was achieved by aligning the single-channel activation curves with corresponding whole-cell tail-activation curves (Section 4B). For all single-channel parameters, and resulting $P_{O,max}$ values, see Section 4D.

4B. Tail activation protocol and analysis
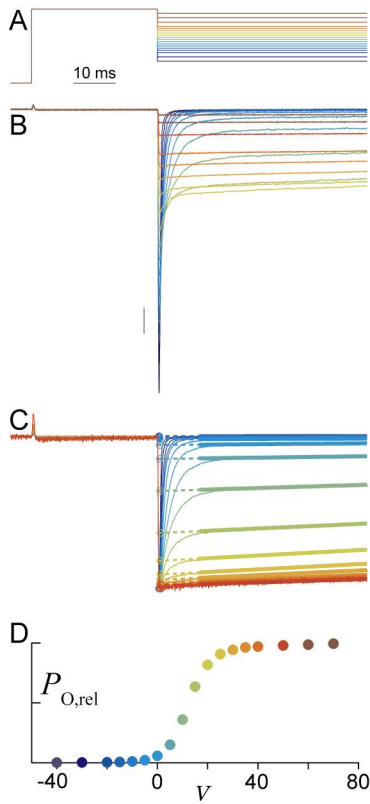
Figure S15. Tail activation protocol. (A) Voltage waveform consists of a step to the reversal potential followed by a step to a family of voltages. (B) Current traces obtained. (C) Currents scaled to tail peak. Solid/dashed lines are used to correct for inactivation. (D) Resulting activation curve calculated by taking the ratio of steady-state current to tail peak. Each round symbol corresponds to voltage waveform and data trace of the same color.

To account for rapid tail kinetics of $Ca_V1.3$ at hyperpolarized voltages, an improved tail-activation protocol was employed as follows (Figure S15A). An activating step to the reversal potential (30 ms at +75 mV for $Ca_V2.2$, 100 ms at +90 mV for $Ca_V1.3$) was followed by a step to a family of voltages. The first step to the reversal potential activated channels to their maximal open probability, $P_{O,max}$. The second voltage transition produced a peak tail current followed by a steady-state current (Figure S15B). Because unitary current is an instantaneous function of voltage, the decay of current during the second step reflects the relaxation of channel open probability from $P_{O,max}$ to the steady-state open probability at the given voltage, $P(V)$. So the ratio of the steady-state current to the peak gives $P_{O,rel}(V) = P(V) / P_{O,max}$. By normalizing each trace to the peak of the tail current (Figure S15C), we can readily appreciate the voltage-dependence of channel activation. $P_{O,rel}$ is plotted as a function of voltage in Figure S15D, where the symbol colors correspond to trace colors above.

For certain constructs, the presence of CDI introduced a slow inactivating component, which interfered with measurement of the steady-state current. To correct for this, a linear relation was optimally fit over the time range +10-100 ms after the final voltage transition (Figure S15C, thick solid lines). The linear fit was extrapolated back (dotted lines) to the time of the tail peak (open circles), and the ratio of this extrapolated value to the peak value was taken as $P_{O,rel}$. Although this procedure effectively corrected for slow CDI, as present in $Ca_V2.2$, it could not correct for fast CDI present in $Ca_V1.3$. To overcome this limitation, we co-expressed $Ca_V1.3$ with CaM_{1234}, a mutant CaM (Peterson et al., 1999) unable to bind Ca^{2+}. We verified that that CaM_{1234} did not influence the activation curve of the channel by comparing the tail-activation in Ba^{2+} with and without CaM_{1234}, which were indistinguishable (data not shown).

This protocol has three key advantages over the traditional tail-activation protocol. First, because $P_{O,rel}$ is calculated from a ratio within a single sweep, it is insensitive to channel rundown. This factors out intra-sweep drift that would undermine the traditional protocol, wherein tail currents are normalized to the maximum across a family of sweeps. Second, since the rising phase of the activation curve is derived from tail repolarizations to relatively positive potentials (comparatively slower gating relaxations), it is possible to resolve the activation curve of rapidly-gating $Ca_V1.3$ channels. Finally, our tail activation protocol involves a pre-pulse to the reversal potential. This mirrors our voltage-block protocol (Section 4C), and thus ideally calibrates channels under the same conditions as voltage block.

Tail activation curves were used to calibrate single-channel data. The maximal open probability was determined by single-channels (tail-activation curves were vertically scaled to match), and the voltage shift was determined by tail-activation (single-channels were horizontally shifted to match). The close correspondence of activation curve shape confirms of the validity of both methods (main paper Figures 3C, 5B, 6A-B, and supplemental data Figures S19A, S19E). For the resulting $P_{O,max}$ values, see Section 4D.

4C. Voltage-block determination of $CDI(\infty)$–P_O relationships

$CDI(\infty)$–P_O relationships (main paper, Figures 3-6) were experimentally determined using a novel voltage-block protocol. Voltage block experiments were performed with a high intracellular concentration of rapid Ca^{2+} chelator (10 mM BAPTA). This ensured that global Ca^{2+} was effectively zero, whereas local calcium spikes remained high ~100 µM (Neher, 1998) (Supplementary Information 3). For all experiments based on $Ca_V1.3$, external solutions contained 40 mM $CaCl_2$ or $BaCl_2$. The high concentration of extracellular Ca^{2+}/Ba^{2+} was chosen to maximize unitary current (large Ca_{spike}). This is relevant for the SQS mechanism, because large Ca_{spike} ensures that $H_{high} \approx 1$, and thus $\langle H(t) \rangle \approx P_O$ (Sections 1A, 1E).

Voltage-block waveforms were specified by the following parameters (Figure S16A; main text Figure 3A):
1) V_U: the 'unblocked' voltage, chosen to maximize P_O while maintaining a large enough unitary current to drive CDI.
2) V_B: the 'blocked' voltage, chosen as the reversal potential.
3) T_G: 'gating' time spent at V_U prior to first block, chosen just long enough to complete activation gating without incurring CDI.
4) T_B: duration of sojourns to V_B.
5) T_U: duration of sojourns to V_U.
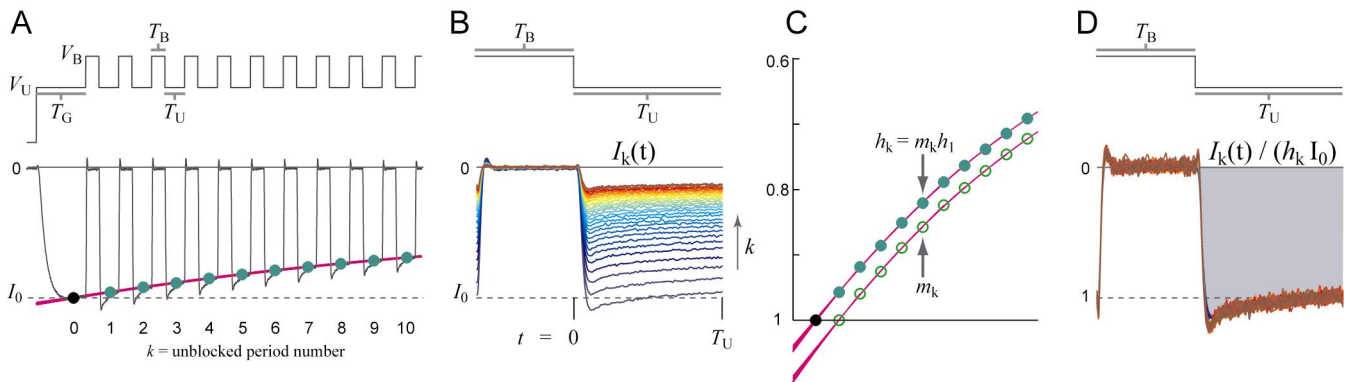
Figure S16. Voltage-block analysis. (A) Whole-cell Ca^{2+} record for exemplar cell on an expanded time base, 40% block condition shown. Voltage waveform (top) with current record (below). Black symbol shows initial peak current. Green symbols plot CDI time course as deduced by algorithm. Definition of unblocked period numbers (bottom). (B) Time-aligned currents for unblocked periods 1 to 100. Every third period is shown. First period is blue, final period is red. (C) Method of deducing time course of CDI. (D) Method of deducing average enhancement of open probability due to sojourns to V_B.

For all experiments, we chose a cycle time, $T_B + T_U = 10$ ms, such that for any desired $P_{O,EFF}$, $T_U = P_{O,EFF} \cdot 10$ ms, $T_B = (1 - P_{O,EFF}) \cdot 10$ ms. The values of V_U, V_B, and T_G were tailored to each construct. Values of V_U were: $Ca_V1.3$, 17 mV; $Ca_V1.3$(high-P_O), 9 mV; $Ca_V2.2$, 21 mV; $\Delta78cBBBBb$, 13 mV. Values of V_B were: $Ca_V1.3/Ca_V1.3$(high-P_O), 90 mV; $Ca_V2.2/\Delta78cBBBBb$, 75 mV. Values of T_G were: $Ca_V1.3/Ca_V1.3$(high-P_O) + CaM_{12}, 5 ms; $Ca_V1.3/Ca_V1.3$(high-P_O) + CaM_{34}, 18 ms; $Ca_V2.2$ (α_{1B}), 30 ms; $\Delta78cBBBBb$, 16 ms.

To minimize a small degree of variability owing to endogenous G-protein and voltage-dependent facilitation, we preceded each sweep with a long (500 ms for $Ca_V1.3$, 50 ms for $Ca_V2.2/\Delta78cBBBBb$) pre-pulse to V_B, followed by a brief (5 ms) return to -90 mV. The pre-pulse did not permit any Ca^{2+}-entry, thus it only served the purpose of 'pre-charging' the channels to their fully open conformation. For all experiments, the holding potential was -90 mV. Voltage-block depolarizations were delivered every 90 s.

To maximize CDI, we utilized step potentials (V_U) just shy of the activation-curve plateau (main paper, Figure 3A, top). This practice produced small current overshoots upon returns to V_U from V_B, which were accounted for in our analysis methodology, as follows. Figure S16A displays a 40% block record from an exemplar cell with an expanded time base. After the initial depolarization to V_U (unblocked period 0), the voltage is repetitively transitioned between V_B and V_U. The current present during each sojourn to V_U (unblocked period 1, 2, 3 …) becomes progressively smaller during each period due to CDI. If each period is superimposed in time (Figure S16B), with the start of each unblocked period aligned to $t = 0$, the current waveform during unblocked period k is described by the function:

$$I_k(t) = N \cdot i \cdot P_k(t) \cdot h_k \tag{4C-1}$$

where N is the number of channels in the cell, i is the unitary current at V_U, $P_k(t)$ is the open probability (of channels not yet inactivated) during unblocked period k, and h_k is the fraction of channels not yet inactivated. Equation 4C-1 pertains to all unblocked periods, with the exception of period 0 (which does not follow a block to V_B). In an ideal experiment, $P_k(t) = P_{O,max}$ (i.e. a constant value), since V_U and V_B should both be on the activation curve plateau (main paper Figure 3A, top). In an actual experiment, however, V_U is just shy of the activation curve plateau. Because of this, $P_k(t)$ will start out near $P_{O,max}$ because the channel had been at V_B prior to the unblocked period, and then drop down slightly because the open probability at V_U may be slightly lower than at V_B. Two points merit emphasis. First, since the voltage block sojourns are repetitive, the slight changes in open probability should repeat during each period, thus $P_k(t)$ should be fairly independent of k. Second, because changes in $P_k(t)$ occur on the millisecond time scale of gating, they can be easily separated from the much slower time course of inactivation. In Figure S16B, the changes in $I_k(t)$ that can be seen during a single unblock period characterize the rapid gating effects of $P_k(t)$, whereas the apparent scaling of $I_k(t)$ with increasing k reflects the slower process of inactivation. Though the absolute amount of inactivation reached by period k ($= 1 - h_k$) is not yet known, the relative degree of inactivation can be determined by scaling the current waveform for period k to that for period 1. Thus,

$$h_k = m_k \cdot h_1 \tag{4C-2}$$

where m_k is calculated by taking the ratio of the average current for unblock period k to that for unblock period 1:

$$m_k = \int_0^{T_U} I_k(t)dt \ / \ \int_0^{T_U} I_1(t)dt \tag{4C-3}$$

Figure S16C plots the time course of m_k (open symbols), where the symbols are horizontally positioned to the center of each unblock period. According to Equation 4C-2, these relative measures of inactivation can be converted to absolute measures if we could estimate h_1, the fraction of channels not yet inactivated by period 1. To estimate h_1, we fit a smooth curve through m_k (Figure S16C, open circles, fit with magenta curve), and extrapolate back to the time of the initial peak. h_1 is estimated as the optimal scaling factor needed to make the extrapolated fit pass through the initial peak (solid black circle). To make this extrapolation more robust, we used a series of smooth fits. The magenta curve in Figure S16C is actually an overlay of 10 fits. These are the best-fit mono-exponential curve to the first 3 points, the first 4 points, the

first 5 points, etc. The estimate of h_1 is based on the average of these fits. Multiplying the open circles (m_k) by h_1 yields the solid green circles (h_k in Figure S16C). These values of h_k, along with the scaled fit are overlaid atop the raw data in Figure S16A. The time course of inactivation, h_k, is thus fully determined.

Beyond calibrating inactivation, this type of analysis also improves the estimate of $P_{O,EFF}$ during voltage block. In our single-channel calibration, we measure the baseline open probability at the unblock voltage, $P_{O/base} = P_O(V_U)$. This calibration is valid for an uninterrupted step (0% block). However, sojourns to V_B (e.g., during 40% block) may cause the open probability to increase above $P_{O/base}$, with fluctuations as characterized by $P_k(t)$. This can be accounted for by describing the initial peak current quantitatively:

$$I_o = N \cdot i \cdot P_{O/base} \tag{4C-4}$$

According to Equations 4C-1 and 4C-4, if we calculate $I_k(t) / (h_k \cdot I_0)$, this should plot $P_k(t) / P_{O/base}$. Figure S16D explicitly performs this operation for all $I_k(t)$, $k \geq 1$. Two points merit discussion. First, the fact that all curves superimpose supports the contention that $P_k(t)$ is independent of k. Second, integrating this waveform (Figure S16D, shaded region) and dividing by T_U (i.e. taking the average of $P_k(t) / P_{O/base}$) yields a factor c, which is the average fold-enhancement in open probability caused by sojourns to V_B. The actual $P_{O,EFF}$ plotted in voltage-block analysis (e.g., main paper Figure 3G) is specified as

$$P_{O,EFF} = \left(P_{O/base} \cdot \frac{T_U}{T_U + T_B} \right) \cdot c \tag{4C-5}$$

Time courses of pure CDI (e.g., main paper Figure 3F) were calculated by taking one minus the ratio of current remaining in Ca^{2+} versus Ba^{2+} (i.e. $1 - h_{k,Ca} / h_{k,Ba}$), averaged over many cells. $CDI(\infty)$–P_O relations (e.g., main paper Figure 3G) were generated by plotting the final time points from the CDI time courses against the average $P_{O,EFF}$ (Equation 4C-5). All average data are presented as mean $\pm$ SEM, calculated, as described, by custom-written software in MATLAB (MathWorks). Because the correction to $P_{O,EFF}$ was minor ($c \approx 1$ in Equation 4C-5), the SEM for $P_{O,EFF}$ was always much smaller than the symbols.

To supplement the high-buffer voltage-block data, we estimated the $P_O = 1$ data point with physiological buffering (0.5 mM EGTA). This allowed a global Ca^{2+} pedestal of ~1-10 µM to accumulate over the duration of a step (Song et al., 1998). In these experiments, we ensured that the amount of divalent (Ca^{2+}/Ba^{2+}) entry into the cell did not overwhelm the divalent buffer in the internal solution. For all traces, we estimated the intracellular rise in divalent concentration by integrating the total current entry into the cell, dividing by a cell volume estimate of ~0.3pL/pF (Satoh et al., 1996), and converting to units of mM. We excluded traces where the estimated rise in divalent concentration was greater than the internal concentration of divalent buffer (Frazier et al., 2000). We also checked for buffer depletion in high-buffer voltage-block experiments by examining currents at the reversal potential of each block cycle. Cells in which we observed an accumulation of outward current during the block sojourns were excluded, as this could be an indication of global divalent accumulation due to consumption of internal buffer.

4D. Fitting
Smooth parametric fits to the N-lobe $CDI(\infty)$–P_O data (main paper Figures 3K, 4G, 5I, 6I) were constrained with the following three considerations in mind: First, because *NSCaTE* has been shown to selectively bind Ca^{2+}/CaM (Dick et al., 2008), mutations to *NSCaTE* should only affect γ, as this corresponds to the channel affinity for Ca^{2+}/CaM. Second, because the amino-terminal *NSCaTE* sequence does not bind apoCaM, and because apoCaM preassociation is believed to occur predominantly on the channel carboxy-terminus (Erickson et al., 2003; Pitt et al., 2001), preassociation should not be affected by mutations to *NSCaTE*.

Thus, all channels based on the same backbone were constrained to the same value of ε. Third, since mutations to *NSCaTE* likely alter the probability of entering the inactivated state without affecting the nature of the inactivated state itself, CDI_{max} (the small open probability while in the inactivated state) is taken to be constant for a given channel backbone. Given these three constraints, all parameters of the SQS analytic relation (main paper Equation 2, with parameters CDI_{max}, ε, and $r = \gamma / \varepsilon$) were highly constrained by our N-lobe voltage-block data. It was not possible to describe our N-lobe block data with any simpler model (for example, a Michaelis-Menton relationship could not fit the data), and the complete set of data could only be fit by the SQS mechanism within a narrow set of parameters. By contrast, the C-lobe voltage-block data was fit well by the slow CaM mechanism (main paper Equation 1); a Michaelis-Menton relation described by the two parameters G and K_{eff}. These two parameters were well constrained by our C-lobe data. Values for single-channel calibration and $CDI(\infty)$–P_O fits are as follows:

Single Channel Parameters
For all constructs, $zF/RT = +12$ mV, as predicted for a divalent cation at room temperature.
For $Ca_V1.3$ and $Ca_V1.3$ (high-P_O), $g=20$ pS, $V_s=31\pm1$ mV.
For $Ca_V2.2$ and cBBBBb, $g=25$ pS, $V_s=59\pm3$ mV.

P_O at V_U was determined for the following constructs:
$Ca_V1.3$: 0.322; $Ca_V1.3$(I48A): 0.318
$Ca_V1.3$(high-P_O): 0.59; $Ca_V1.3$(high-P_O, I48A): 0.61
$Ca_V2.2$: 0.51;   cBBBBb: 0.64.

N-lobe CDI:

$Ca_V1.3$:	$CDI_{max}=0.68$;	$\varepsilon=80$;	native $\gamma=435$;	R52A $\gamma=158$;	I48A $\gamma=55$;	W44A $\gamma=3$
$Ca_V1.3$(high-P_O):	$CDI_{max}=0.83$;	$\varepsilon=80$;	native $\gamma=144$;	R52A $\gamma=80$;	I48A $\gamma=17$;	W44A $\gamma=6$
$Ca_V2.2$:	$CDI_{max}=1$;	$\varepsilon=30$;	native $\gamma=7.5$;			
$\Delta78$cBBBBb:	$CDI_{max}=1$;	$\varepsilon=30$;	native $\gamma=137$;			W82A $\gamma=30$

C-lobe CDI:

|			
$Ca_V1.3$:	$G=0.75$	native $K_{eff}=0.028$	I48A $K_{eff}=0.028$
$Ca_V1.3$(high-P_O):	$G=0.83$	native $K_{eff}=0.051$	

4E. Statistical assessment of upward curvature

In Section 1, we proved that the SQS mechanism is capable of generating $CDI(\infty)$–P_O relationships with upward curvature, and that this curvature distinguishes the SQS mechanism from among a large class of alternatives. Experimental resolution of upward curvature therefore provides the strongest evidence for the SQS mechanism. In this work, we experimentally resolved upward curvature ($r < 1$) in four constructs. Here the statistical strength of this upward curvature is quantified (Figure S17).

First, we considered both the voltage-block and low-buffer data (Figures S17A-D, left plots). For each construct, we compared the 'goodness of fit' of the SQS relation (green or magenta curve) to a simple linear relation (black line). The SQS fits correspond to main paper Equation 2 with parameters as in Section 4D. The linear fits are constrained through (0, 0) with slopes chosen to minimize the chi-squared error. For each construct, we compared the two fits by taking a ratio of their summed chi-squared errors, yielding an F-value. The F-values could then be compared to an F-distribution, yielding p-values, which are shown in Figures S17A-D (left plots). The p-values can be interpreted as the probability that the data arises from a mechanism with a linear $CDI(\infty)$–P_O relation, rather than an upwardly-curved SQS relation. Thus, the smaller the p-value, the more certain we can be that the data statistically exhibits upward

curvature and supports the SQS mechanism. Of four constructs with $r < 1$, three had significant upward curvature—$Ca_V2.2$, $Ca_V1.3$(high-P_O, I48A), and $Ca_V1.3$(high-P_O, W44A) (Figures S17B-D, left plots).

Though compelling, this initial analysis includes the physiological-buffer estimates of CDI at $P_O = 1$. The SQS analytic equation (main paper, Equation 2) is strictly derived under conditions of high-buffering. Though CDI under physiological buffering should serve as a lower-limit estimate of CDI under high-buffering at $P_O = 1$ (see main paper, discussion of Figure 2G), such reasoning is subject to some underlying assumptions. The most stringent verification of the SQS mechanism therefore requires experimental resolution of upward curvature using only the high-buffer voltage-block data. The statistical comparison of the SQS fits to linear fits was repeated using only the high-buffer data (Figures S17A-D, right plots). The SQS fits (green or magenta curves) were the same as before, but the linear fits (blue lines) were re-optimized to the five high-buffer data points. Even under this more stringent analysis, two constructs had statistically significant upward curvature—$Ca_V1.3$(high-P_O, I48A), and $Ca_V1.3$(high-P_O, W44A) (Figures S17C-D, right plots). The most compelling resolution of upward curvature was for the $Ca_V1.3$(high-P_O, I48A) construct, which had a p-value of 0.003. Accordingly, the data is 99.7% more likely for an SQS mechanism than a mechanism which exhibits a linear $CDI(\infty)$–P_O relationship.
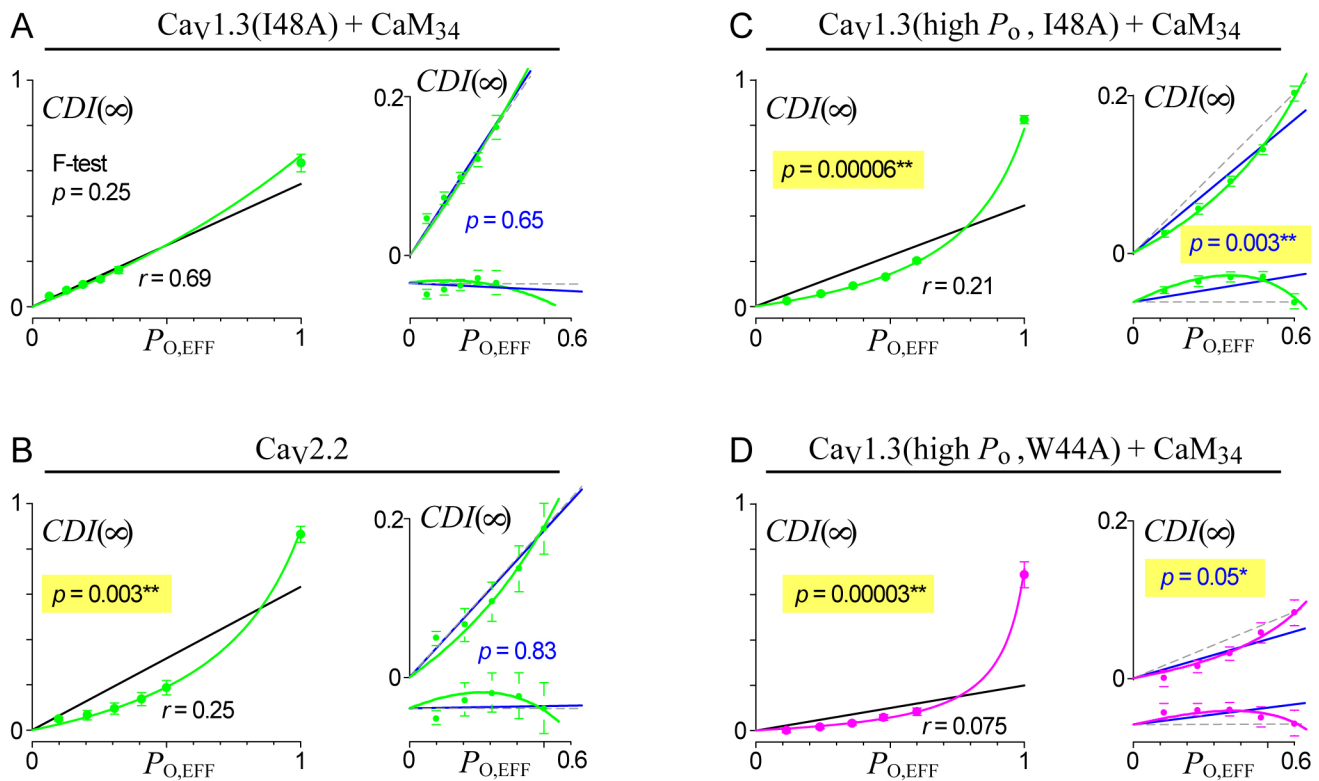
Figure S17. Statistical assessment of Upward Curvature.
(A-D, left plots) Statistical comparison of SQS fits with linear fits for the four constructs exhibiting upward curvature ($r < 1$). Both voltage-block and low-buffer data are included in this analysis. Error bars show SEM. The SQS fits are the green/magenta curves (color scheme as in main paper). The linear fits (minimum chi-squared error to all six data points) are the black lines. F-test statistic (p-values) shown. All p-values that are statistically significant are highlighted in yellow.
(A-D, right plots) Similar analysis using only the high-buffer data, shown on an expanded vertical scale. Here the optimum linear fits to the five high-buffer data points are shown in blue, with the F-test p-values showing the comparison of SQS and linear fits to the high-buffer data only. Plots at the bottom of each panel show the degree to which the data and the fits undershoot the dashed gray line, which was chosen to pass through the 0% block data. All p-values that are statistically significant are highlighted in yellow, indicating statistically significant upward curvature under high-buffering.

4F. Continuum numerical simulations (main text Figures 2C, G)

Numerical simulations (main text Figures 2C, G) were performed in MATLAB (MathWorks, Natick, MA). Because Ca(t) is approximated as a square-pulse train (Supplementary Information 3), the time-varying rate constant for transition from state 2 to 3 ($= k_{on} \cdot Ca^2(t)$ in main text Figure 2A), is actually fixed for the duration of each channel opening or closing. Thus, the time-evolution of state occupancy over the duration of a channel opening or closing could be calculated via multiplication with the matrix exponential of the state-transition matrix. Given initial occupancy in state 1, successive matrix multiplication for each opening/closing yielded the time-evolution of CDI (state 4).

More explicitly, the following equations were used. Initially, all systems occupied state 1:

$$P(0) = \begin{bmatrix} 1 & 0 & 0 & 0 \end{bmatrix} \tag{4F-1}$$

where the elements of P are the probabilities of occupying states 1, 2, 3 and 4. Note that the elements of P must sum to 1.

The time-evolution of state occupancy over the duration of a first opening (that starts at t and ends at $t + t_{open}$) was then calculated by:

$$P(t + t_{open}) = \text{expm}\left(t_{open} \cdot \begin{bmatrix} -b & a & 0 & 0 \\ b & -a - k_{on} \cdot (Ca_{spike} + Ca_{global})^2 & k_{off} & 0 \\ 0 & k_{on} \cdot (Ca_{spike} + Ca_{global})^2 & -k_{off} - \alpha & \beta \\ 0 & 0 & \alpha & -\beta \end{bmatrix} \right) \cdot P(t) \tag{4F-2}$$

where expm indicates the matrix exponential.

The time-evolution of state occupancy over the duration of a subsequent closing (that starts at t^* and ends at $t^* + t_{closed}$) was then calculated by:

$$P(t^* + t_{closed}) = \text{expm}\left(t_{closed} \cdot \begin{bmatrix} -b & a & 0 & 0 \\ b & -a - k_{on} \cdot Ca_{global}^2 & k_{off} & 0 \\ 0 & k_{on} \cdot Ca_{global}^2 & -k_{off} - \alpha & \beta \\ 0 & 0 & \alpha & -\beta \end{bmatrix} \right) \cdot P(t^*) \tag{4F-3}$$

Equations 4F-2 and 4F-3 were then used iteratively to yield the time-evolution of CDI, which is shown as a plot of the fourth element of $P(t)$ versus time. A similar approach was used for the simulations involving 6 states (Supplementary Information 1F) and 5 states (Supplementary Information 3D).

5. Supplemental Data

5A. Further *NSCaTE* mapping data for main paper, Figure 4

To experimentally adjust the SQS parameter *r*, the *NSCaTE* region of $Ca_V1.3$ was scanned with single alanine point mutations (Figure 4A of the main text, Figure S18). Functional effects were determined through whole-cell electrophysiology recordings (Figure S18A), which quantify CDI under high buffering. The binding affinity was probed utilizing a FRET 2-hybrid assay (Figure S18B-C), in which amino-terminal fragments of $Ca_V1.3$ containing *NSCaTE* were fused to ECFP and co-transfected with CaM fused to EYFP. Concentration-dependent spurious FRET was corrected (Stratton et al., 2004) and the relative dissociation constant $K_{d,EFF}$ was determined as described (Erickson et al., 2001; Erickson et al., 2003). Briefly, the FRET Ratio (*FR*), defined as the fractional increase in YFP emission due to FRET interaction, was calculated from

$$FR = [S_{FRET} - R_{D1} \cdot S_{CFP}] / [R_{A1} \cdot (S_{YFP} - R_{D2} \cdot S_{CFP})]$$

where S_X indicates the fluorescence measurement with a given filter cube *X* (= CFP, FRET, and YFP cubes). R_{D1} and R_{A1} are optical calibration constants, which were determined for our setup. *FR* = 1 in the absence of FRET, and increases linearly with rising FRET efficiency (*FR* = 5.3 at 25% FRET efficiency).

FR was obtained from multiple cells, and cell-to-cell variation in expression levels permitted resolution of $K_{d,EFF}$ and FR_{max} via binding-curve analysis (Erickson et al., 2001; Erickson et al., 2003). Figures S18B and S18C show the FRET binding curves for the various FRET pairings, and Table S3 shows the deduced binding curve parameters. Of note, there was no detectible interaction (*FR* ≈ 1) between apoCaM and either the intact *NSCaTE* or the I48A mutant (blue data points in Figure S18B, and values in Table S3). By contrast, there was strong interaction between *NSCaTE* and Ca^{2+}/CaM (red data points in Figure S18B, and values in Table S3). These outcomes support the claim that *NSCaTE* selectively interacts with Ca^{2+}/CaM.

FRET Partner	Construct Name	Construct Source	aa range	mean FR	SEM	Ncell	KdEFF x 1000	FRmax
apoCaM	NT-D	alpha 1D	35-94	1.08	0.03	16	9696	9.30
apoCaM	NT-D I48A	alpha 1D	35-94	1.04	0.06	10	26246819	9.30
Ca2+/CaM	NT-D	alpha 1D	35-94	5.00	0.33	67	23	7.48
Ca2+/CaM	NT-D W44A	alpha 1D	35-94	1.1230291	0.114336	14	4033	9.30
Ca2+/CaM	NT-D Q45A	alpha 1D	35-94	6.5635077	0.151063	22	8	7.48
Ca2+/CaM	NT-D I48A	alpha 1D	35-94	4.3526112	0.29205	43	52	8.76
Ca2+/CaM	NT-D D49A	alpha 1D	35-94	6.2330433	0.286816	26	20	8.59
Ca2+/CaM	NT-D R52A	alpha 1D	35-94	3.57	0.207795	31	48	6.32
Ca2+/CaM	NT-D Q53A	alpha 1D	35-94	6.5346921	0.21697	21	10	7.85
Ca2+/CaM34	NT-D	alpha 1D	35-94	4.3644147	0.15881	31	9	5.27
Ca2+/CaM34	NT-D W44A	alpha 1D	35-94	1.54	0.085624	28	1867	9.30
Ca2+/CaM34	NT-D I48A	alpha 1D	35-94	3.4103868	0.198048	28	64	5.30
Ca2+/CaM34	NT-D R52A	alpha 1D	35-94	4.0465346	0.160142	29	22	5.33

Table S3. Here we list the full set of parameter values obtained for the FRET experiments shown in Figure S18(B-C), which are plotted as bar graphs in main paper, Figures 4B-C.
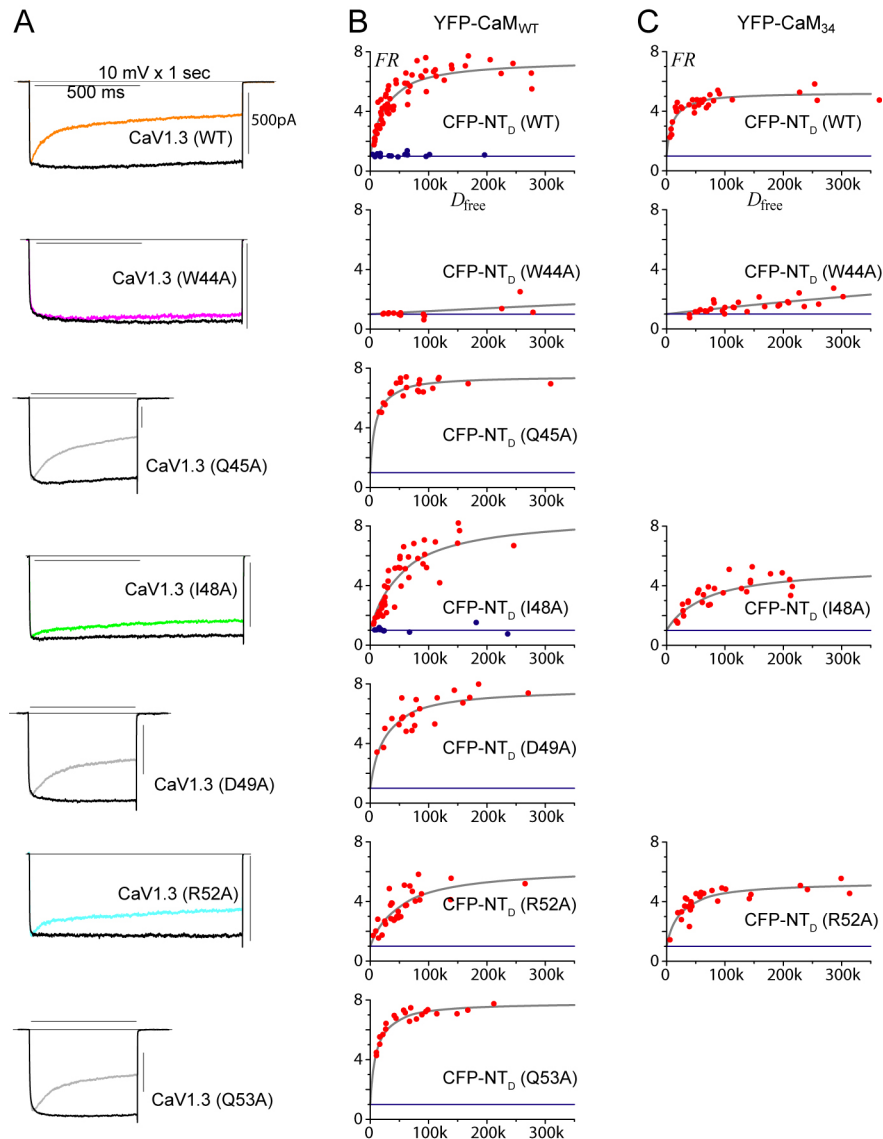
Figure S18. Data supporting the *NSCaTE* alanine scan of main paper Figures 4, A-C.

(A) Whole-cell recordings of $Ca_V1.3$ (top row) and *NSCaTE* point mutants (below) in 10 mM BAPTA. Traces show Ca^{2+} currents (colored or gray) overlaid with Ba^{2+} currents (black) in response to depolarizations to 10 mV. Time bar, 500 ms, current bar, 1 nA, referenced to Ca^{2+} trace. Ba^{2+} currents reduced by 2-3x to enable direct comparison with Ca^{2+}. CDI can be quantified by the difference in the fraction of current remaining in Ba^{2+} versus Ca^{2+} after 500 ms.

(B-C) Exemplar FRET two-hybrid binding curves delineating $K_{d,EFF}$. YFP–CaM_{WT} (B) or YFP–CaM_{34} (C) is pitted against $Ca_V1.3$ (α_{1D}) amino-terminal constructs tagged with CFP. The CFP-channel fragments contain *NSCaTE* (top row) and *NSCaTE* with single alanine point mutants (all other rows below). The red symbols indicate data obtained in elevated Ca^{2+}, and the blue symbols indicate resting Ca^{2+} conditions.

5B. Supplemental Ca$_V$1.3 single-channel and voltage-block data
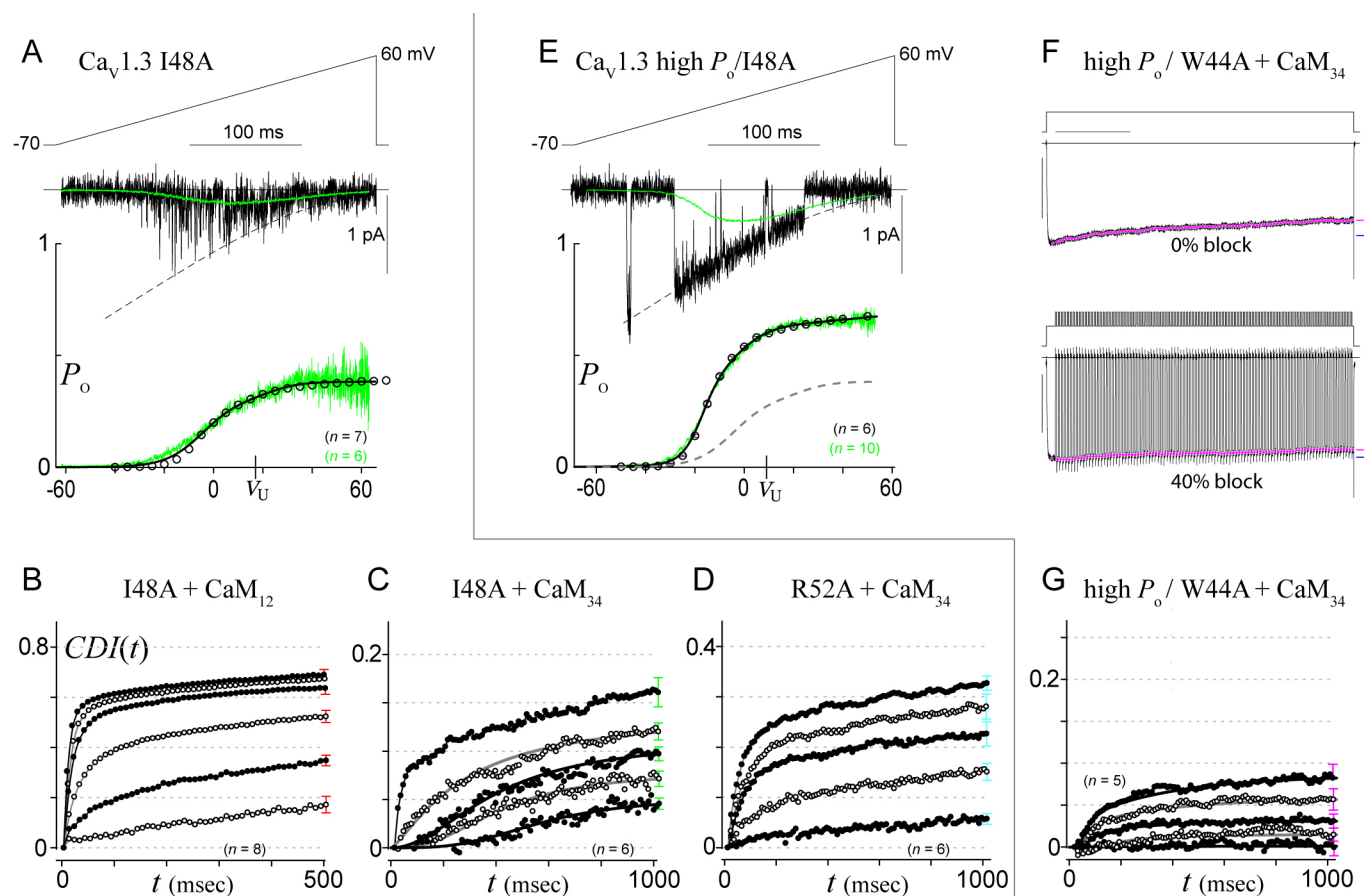
Figure S19. Ca$_V$1.3 data supporting voltage-block analysis of main paper Figures 4-5.

Panels in support of main paper Figure 4:
(A) Single-channel analysis of I48A mutant is indistinguishable from the native Ca$_V$1.3 (main paper Figure 3C).
(B) Time course of C-lobe CDI (isolated with CaM$_{12}$) for the I48A mutant. Format as in main paper Figure 3F. This data corresponds to main paper Figures 4D-E.
(C-D) Time course of N-lobe CDI (isolated with CaM$_{34}$) for Ca$_V$1.3 *NSCaTE* mutants. Format as in main paper Figure 3J. The I48A data in panel (C) corresponds to main paper Figure 4F-G (green). The R52A data in panel (D) corresponds to main paper Figures 4H, G (cyan).

Panels in support of main paper Figure 5:
(E) Single-channel analysis of high-P_O/I48A is indistinguishable from high-P_O with native *NSCaTE* from main paper Figure 5B. Dashed curve reproduces the relation from (A).
(F-G) Voltage-block exemplar traces (F) and time course (G) for N-lobe CDI (isolated with CaM$_{34}$) of high-P_O/W44A. This data supports main paper Figure 5I (magenta), and supplementary Figure S17D.

Supplemental References

Bayley, P., Ahlstrom, P., Martin, S. R., and Forsen, S. (1984). The kinetics of calcium binding to calmodulin: Quin 2 and ANS stopped-flow fluorescence studies. Biochem Biophys Res Commun *120*, 185-191.

Dick, I. E., Tadross, M. R., Liang, H., Tay, L. H., Yang, W., and Yue, D. T. (2008). A modular switch for spatial Ca^{2+} selectivity in the calmodulin regulation of Ca_V channels. Nature *451*, 830-834.

Erickson, M. G., Alseikhan, B. A., Peterson, B. Z., and Yue, D. T. (2001). Preassociation of calmodulin with voltage-gated Ca(2+) channels revealed by FRET in single living cells. Neuron *31*, 973-985.

Erickson, M. G., Liang, H., Mori, M. X., and Yue, D. T. (2003). FRET two-hybrid mapping reveals function and location of L-type Ca2+ channel CaM preassociation. Neuron *39*, 97-107.

Frazier, C. J., George, E. G., and Jones, S. W. (2000). Apparent change in ion selectivity caused by changes in intracellular K(+) during whole-cell recording. Biophys J *78*, 1872-1880.

Hille, B. (1984). Ionic channels of excitable membranes (Sunderland, MA, Sinauer Associates).

Houdusse, A., Gaucher, J. F., Krementsova, E., Mui, S., Trybus, K. M., and Cohen, C. (2006). Crystal structure of apo-calmodulin bound to the first two IQ motifs of myosin V reveals essential recognition features. Proc Natl Acad Sci U S A *103*, 19326-19331.

Imredy, J. P., and Yue, D. T. (1994). Mechanism of Ca^{2+}-sensitive inactivation of L-type Ca^{2+} channels. Neuron *12*, 1301-1318.

James, P., Vorherr, T., and Carafoli, E. (1995). Calmodulin-binding domains: just two faced or multi-faceted? Trends in Biochemical Sciences *20*.

Kerr, R. A., Bartol, T. M., Kaminsky, B., Dittrich, M., Chang, J. J., Baden, S. B., Sejnowski, T. J., and Stiles, J. R. (submitted). Fast Monte Carlo simulation methods for biological reaction-diffusion systems in solution and on surfaces.

Kits, K. S., de Vlieger, T. A., Kooi, B. W., and Mansvelder, H. D. (1999). Diffusion barriers limit the effect of mobile calcium buffers on exocytosis of large dense cored vesicles. Biophys J *76*, 1693-1705.

Martin, S. R., Andersson Teleman, A., Bayley, P. M., Drakenberg, T., and Forsen, S. (1985). Kinetics of calcium dissociation from calmodulin and its tryptic fragments. A stopped-flow fluorescence study using Quin 2 reveals a two-domain structure. Eur J Biochem *151*, 543-550.

Neher, E. (1998). Vesicle pools and Ca^{2+} microdomains: new tools for understanding their roles in neurotransmitter release. Neuron *20*, 389-399.

Neher, E., and Steinbach, J. H. (1978). Local anaesthetics transiently block currents through single acetylcholine-receptor channels. J Physiol *277*, 153-176.

Peterson, B. Z., DeMaria, C. D., Adelman, J. P., and Yue, D. T. (1999). Calmodulin is the Ca^{2+} sensor for Ca2+ -dependent inactivation of L- type calcium channels. Neuron *22*, 549-558.

Pitt, G. S., Zuhlke, R. D., Hudmon, A., Schulman, H., Reuter, H., and Tsien, R. W. (2001). Molecular basis of calmodulin tethering and Ca2+-dependent inactivation of L-type Ca2+ channels. J Biol Chem *276*, 30794-30802.

Satoh, H., Delbridge, L. M., Blatter, L. A., and Bers, D. M. (1996). Surface:volume relationship in cardiac myocytes studied with confocal microscopy and membrane capacitance measurements: species-dependence and developmental effects. Biophys J *70*, 1494-1504.

Schnee, M. E., and Ricci, A. J. (2003). Biophysical and pharmacological characterization of voltage-gated calcium currents in turtle auditory hair cells. J Physiol *549*, 697-717.

Sherman, A., Keizer, J., and Rinzel, J. (1990). Domain model for Ca2(+)-inactivation of Ca2+ channels at low channel density. Biophys J *58*, 985-995.

Smith, G. D. (2001). Modeling Local and Global Calcium Signals Using Reaction-Diffusion Equations. In: Computational Neuroscience: Realistic Modeling for Experimentalists, ed. De Schutter, E (Boca Raton, Fla., CRC Press).

Song, L. S., Sham, J. S., Stern, M. D., Lakatta, E. G., and Cheng, H. (1998). Direct measurement of SR release flux by tracking 'Ca^{2+} spikes' in rat cardiac myocytes. J Physiol (Lond) *512*, 677-691.

Stern, M. D. (1992). Buffering of calcium in the vicinity of a channel pore. Cell Calcium *13*, 183-192.

Stiles, J., and Bartol, T. (2001). Monte Carlo methods for simulating realistic synaptic microphysiology using MCell. In: Computational Neuroscience: Realistic Modeling for Experimentalists, ed. De Schutter, E (Boca Raton, Fla., CRC Press).

Stiles, J. R., Van Helden, D., Bartol, T. M., Jr., Salpeter, E. E., and Salpeter, M. M. (1996). Miniature endplate current rise times less than 100 microseconds from improved dual recordings can be modeled with passive acetylcholine diffusion from a synaptic vesicle. Proc Natl Acad Sci U S A *93*, 5747-5752.

Stratton, J., Evans, J., Erickson, M. G., Alvania, R. S., and Yue, D. T. (2004). The nature of concentration-dependent spurious FRET arising from CFP and YFP (abstr.). Biophys J *86*, 317a.

Teleman, A., Drakenberg, T., and Forsen, S. (1986). Kinetics of Ca^{2+} binding to calmodulin and its tryptic fragments studied by 43Ca-NMR. Biochim Biophys Acta *873*, 204-213.